Theorizing Hidden Chemical and Magnetic Order in Alloys

By

Flynn Walsh

A dissertation submitted in partial satisfaction of the

requirements for the degree of

Doctor of Philosophy

in

Applied Science & Technology

in the

Graduate Division

of the

University of California, Berkeley

Committee in charge:

Professor Mark Asta, Chair
Professor Daryl Chrzan
Professor Robert O. Ritchie

Summer 2023

Abstract

Theorizing Hidden Chemical and Magnetic Order in Alloys

By

Flynn Walsh

Doctor of Philosophy in Applied Science & Technology

University of California, Berkeley

Professor Mark Asta, Chair

The popularization of concentrated solid-solution alloys has prompted a renewed search for atomic-scale chemical order among elements that appear randomly distributed within crystal lattices. However, confounding signals in electron diffraction experiments necessitate an immediate reliance on indirect measurements for detecting local order in compositionally complex alloys, as may be interpreted through computer simulations. For instance, both the structure and magnetization of the CrCoNi model system notably contradict *ab initio* theory for random alloys, but could be reconciled by the widespread presence of chemical short-range order. These simulations additionally find significant magnetic interactions in materials that are often assumed only paramagnetic, motivating further predictions of antiferromagnetism in binary Cr-Ni alloys, which are conventionally understood to have nonmagnetic ground states. This result indicates either the failure of standard theories or, as suggested by anomalous historical measurements, the existence of previously overlooked magnetic order that could persist well above ambient temperatures. In order to realistically model magnetic thermodynamics, a new Monte Carlo approach is developed and found to provide insight into the origin and prevalence of magnetic short-range order.

Contents

Chapter 1

Overview of the dissertation

Most of the work described in this dissertation was carried out as part of the Damage-Tolerance in Structural Materials program in the Materials Sciences Division of Lawrence Berkeley National Laboratory, although a fellowship allowed me to explore some more fundamental aspects of modeling magnetism. Our program seeks to understand the origins of the unprecedented combinations of strength and toughness observed in certain complex concentrated alloys (CCAs), with my work focusing on face-centered cubic (fcc) systems consisting of several $3d$ transition metals.

While many mechanical properties are ultimately dictated by mesoscale phenomena, we have been developing a hypothesis that the remarkable postyield damage-tolerance of this class of nominally disordered materials originates from a sequence of deformation mechanisms that is affected by atomic-scale chemical order among the constituent elements. This form of chemical rearrangement can be challenging to detect, inviting a tantalizing search for elusive short-range order (SRO) in ostensibly "high-entropy" environments.

As an introduction, Ch. 2 reviews some of the basic principles of chemical SRO from a historical perspective. This work will be published as the first half of Ref. [1]. Ch. 3 addresses recent attempts to characterize SRO by transmission electron microscopy (TEM), which, unfortunately, appear to have been measuring something else instead. This chapter will be published as Ref. [2].

As these TEM studies constitute the majority of contemporary characterization efforts, their refutation leaves an immediate lack of experimental clarity on conventionally processed material. Ch. 2 discusses how the presence of SRO may still be inferred by comparing indirect measurements to theoretical predictions. In this manner, Ch. 4 chronicles an investigation of SRO in the CrCoNi model system using spin-polarized density-functional theory (DFT), based on work published in Ref. [3], with discussion drawing from Ref. [1]. It is argued that a significant degree of SRO may be ubiquitous in this system and other related alloys containing concentrated Cr or V.

Intriguingly, magnetism was found to play a role in ground-state calculations of ordering in CrCoNi, although it is unclear if this prediction is physically reasonable. As the possibility of magnetic order in many-component alloys is complicated by uncertain chemical

structures, Ch. 4 explores the basic predictions of the theory in related but considerably better studied binary Cr-Ni alloys, which are traditionally considered to be only paramagnetic. Remarkably, conventional DFT is found to consistently predict antiferromagnetism in at least the chemically ordered phases of the system. Although this result could indicate a failure of the theory, it is proposed that the presence of hidden antiferromagnetic order could be consistent with a number of anomalous historical measurements, motivating future experiments. This chapter was published as Ref. [4].

While these works only consider magnetic ground states, proper treatment of magnetism requires the simulation of finite-temperature ensembles, which are commonly parameterized by classical Heisenberg models. However, widely employed classical sampling procedures poorly describe magnetic phenomena due to the quantum nature of spins. Addressing this problem, Ch. 6 describes a new method for sampling spin states that provides accuracy comparable to existing workarounds with significantly improved generality and convenience, as published in Ref. [5].

Chapter 2

Introduction to short-range order

2.1 Binary alloys

Before considering chemical short-range order (SRO) in many-component systems, it is helpful to review the physics of chemical rearrangement in binary solid solutions, of which there are two distinct forms. In the first, two elements may simply segregate, or "cluster," forming separate phases in the long-range limit. Alternatively, attractive interactions between unlike atomic species may lead to the formation of various periodic lattice decorations, or orderings.

In either case, atomic distributions are traditionally described in terms of the frequencies of chemical pairs. The likelihood of finding elements i and j at neighbor separation $\boldsymbol{r}_p$ is expressed by the Warren-Cowley (WC) parameter $\alpha_{ij}^{(p)}$. In a random solution, the probability of finding j at a site $\boldsymbol{r}_p$ from i is simply the fractional concentration of j, $c_j = 1 - c_i$. For actual probability $P_p(j \mid i)$, the WC parameter may be defined for any[1] i and j as

$$\alpha_{ij}^{(p)} = \alpha_{ji}^{(p)} = 1 - \frac{P_p(j \mid i)}{c_j}. \tag{2.1}$$

Negative $\alpha_{ij}^{(p)}$ values indicate more ij-type p-pairs than in a random alloy, in which all $\alpha_{ij}^{(p)} = 0$, while positive values mean the opposite. Considering unlike nearest-neighbor pairs, $\alpha_{ij}^{(1)} > 0$ suggests clustering, while $\alpha_{ij}^{(1)} < 0$ typically indicates ordering.

The magnitude of $\boldsymbol{r}_p$ at which $\alpha_{ij}^{(p)}$ becomes indistinguishable from zero may be termed the *correlation distance*, which is arbitrarily large in the case of long-range order (LRO) or phase separation. SRO has by definition a measurably finite correlation distance, although $\alpha_{ij}^{(p)}$ typically decays slowly enough that it is more convenient to represent ordering in reciprocal space via the Fourier transformation of WC parameters. In this picture, mean chemical distributions are described in terms of wave vectors, $\boldsymbol{k}$, associated with amplitudes that may

[1] Some popular definitions of the parameter [6] define $\alpha_{ii}^{(p)}$ differently, inverting the meaning of the sign relative to $\alpha_{i\neq j}^{(p)}$.

be defined[2] as

$$Q_{ij}(\boldsymbol{k}) = \frac{c_i}{c_i - \delta_{ij}} \sum_p \alpha_{ij}^{(p)} \exp\left(-i\,\boldsymbol{k}\cdot\boldsymbol{r}_p\right). \tag{2.2}$$

For the binary alloy depicted in Fig. 2.1(b), panel (c) shows Q_{ij} for the (001) plane.

While somewhat less immediately intuitive, the reciprocal-space view is attractive because binary $Q_{ij}(\boldsymbol{k})$ is closely related to measurable diffuse scattering intensity, as will be discussed later. Many structures may also be succinctly described by a small number of wave vectors. Clustering, for instance, is associated with $\boldsymbol{k}$ approaching (000), which corresponds to perfect phase separation.

Nonzero values of $\boldsymbol{k}$ represent ordering, which may be interpreted in terms of concentration waves expressing the average chemical environment of a crystal. For a site at $\boldsymbol{r}$, the probability of finding either element is a superposition of waves $\sim e^{i\boldsymbol{k}\cdot\boldsymbol{r}}$ with weights related to $Q_{ij}(\boldsymbol{k})$ [7–9]. While SRO necessarily involves many periodicities, specific wave vectors associated with LRO structures are generally dominant.

2.2 Many-component alloys

This method of binary pair analysis may be applied to many-component systems, at the expense of some elegance; $Q_{ij}(\boldsymbol{k})$ is no longer directly measurable and the complete determination of ordering waves requires system-specific analysis [10]. Still, the theoretical SRO of M-component CCAs is often described in terms of $M(M-1)/2$ correlations between unlike pairs, in real ($\alpha_{ij}^{(p)}$) or reciprocal ($Q_{ij}(\boldsymbol{k})$) space.

In many systems, however, it may be simpler and more intuitive to first consider M (or even $M-1$) like-pair terms, i.e. α_{ii} or Q_{ii}. In contrast to unlike pairs, the average distribution of individual element i may still be interpreted in terms of a superposition of concentration waves[3] with weights related to $Q_{ii}(\boldsymbol{k})$. These values are also simpler to determine experimentally [6].

Despite greater compositional complexity, the ordering of many recently studied CCAs appears to primarily involve segregation or sublattice formation by a single element. A system may exhibit multiple such processes, including the formation of complex LRO from the sequential development of sublattices, but individual ordering reactions are often, though by no means always, associated with one chemical species. As a hypothetical example, a model CCA containing both ordering and clustering elements is depicted in Fig. 2.1(d).

Due to the interdependence of pair correlations, the clustering or ordering of a single element is redundantly reflected in many separate pair parameters. For example, the formation of a Cr sublattice in CrFeCoNi is similarly apparent in the Cr-Fe, Cr-Co, and Cr-Ni pair correlations [11], but could be approximately described by the distribution of Cr-Cr pairs.

[2] The prefactor, which cancels for $i \neq j$, recovers the standard expression for Q_{ij} [6] for the definition of α_{ij} in Eq. (2.1).

[3] Albeit, without the phase that indicates the distribution relative to other species.

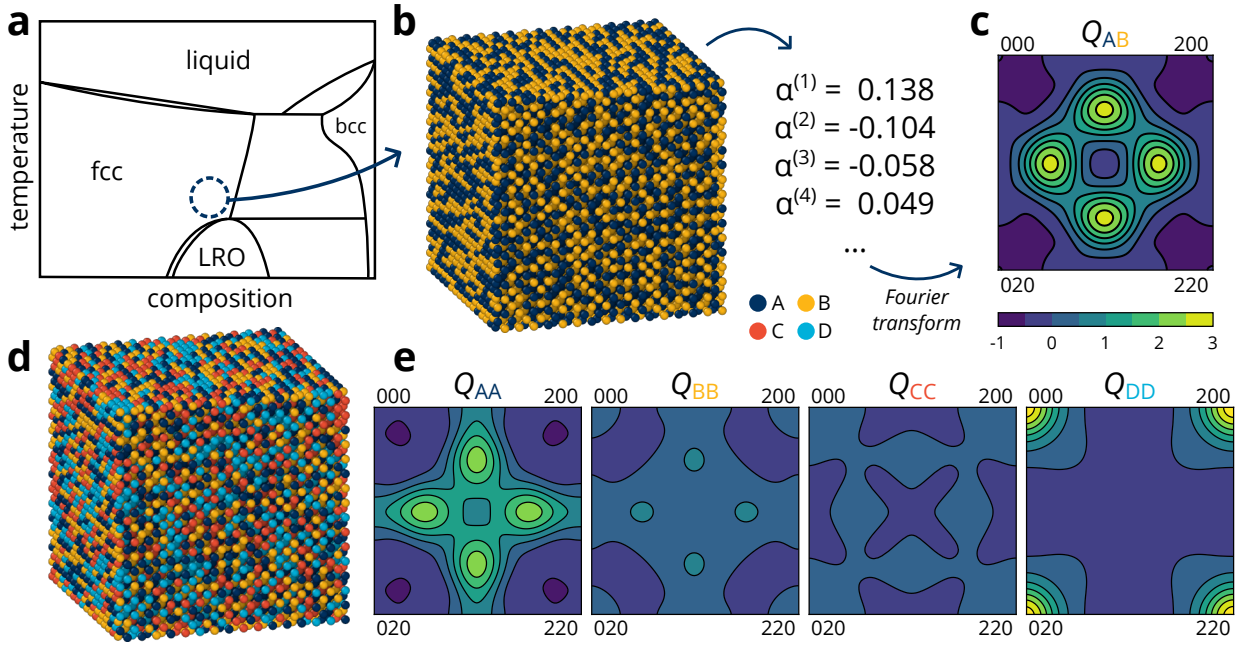

Figure 2.1: (a) Phase diagram of a model binary ordering alloy. A hypothetical chemical structure from the highlighted region is depicted in (b), with WC parameters determined from Eq. (2.1). (c) The same ordering represented in the (001) plane of reciprocal space via Eq. (2.2). (d) Real- and (e) reciprocal-space representation of equilibrium SRO/C in a model quaternary alloy. Element A (dark blue) exhibits ordering tendencies associated with the wave vector $\boldsymbol{k} = (1\frac{1}{2}0)$, while element D (light blue) appears to cluster ($\boldsymbol{k} \to (000)$); elements B (gold) and C (red) are more randomly distributed.

The theoretical SRO of nearest neighbors in CrCoNi appears similarly determined by the frequency of Cr-Cr bonds; Ni-Ni and Co-Co correlations remain small and remaining values largely conserve probability [3, 12].

Of course, specific CCAs will likely display novel ordering phenomena that may require the full picture of concentration waves [9, 10] or even many-body WC parameters [13]. The interpretability of all mean-field descriptions can also be compromised by the formation of local compositional heterogeneity in complex alloys. Nonetheless, the analysis of individual species in the binary formalism provides an intuitable starting point that invites the application of various historical results.

2.3 Phase transitions

At some sufficiently low temperature, T_{tr}, the interactions driving ordering or clustering induce a phase transition, below which the *equilibrium* correlation distance becomes arbitrarily long-ranged. Below T_{tr}, equilibrated clustering becomes phase separation and SRO gives way to LRO. The microstructure of real alloys, however, often corresponds not to an equilibrium configuration, but rather an arrested phase transition, such as partial phase separation into intermediate-sized clusters. In many popular $3d$ systems, LRO develops very slowly and in some cases appears practically limited to nanoscale antiphase domains [14]. While this form of order remains fundamentally short-ranged, it may also be considered incomplete LRO to distinguish from the equilibrium SRO found above T_{tr}.

Incomplete LRO, which is often controllable through heat treatments, has been the focus of most historical [15–17] and many recent [11, 18, 19] studies on SRO. While tuning order in this manner could in principle enable the tailoring of material properties, most alloys are not processed in any way intended to promote ordering. Equilibrium short-range order or clustering (SRO/C) may nonetheless form as samples are cooled from high temperatures, e.g. in the region of the phase diagram highlighted in Fig. 2.1(a). The prevalence of this type of SRO, which may be further enhanced upon initial cooling below T_{tr} [20], is considered in Ch. 4.

It should be noted that the structure approached by the SRO forming above T_{tr} can differ from the LRO found below T_{tr}, even though the interactions driving chemical rearrangement are typically equivalent. As dictated by Landau's theory of phase transitions, crystallographic considerations require that many LRO structures form by first-order phase transitions, which generally involve nucleation and growth processes that impose energy barriers on the initial stages of ordering. For these structures, the incomplete forms of order that could occur above T_{tr} may be energetically unfavorable [8, 21].

Certain other decorations can form without any such barriers by continuous (second-order) phase transitions. In the picture of concentration waves, the SRO forming above T_{tr} may be associated with the wave vectors of these structures, even if their long-ranged forms are never realized. Of course, high-temperature SRO typically shares key features with the LRO ground state, such as the minimization of same-species nearest neighbors. The Cr-Ni system clearly demonstrates this phenomenon; $CrNi_2$ alloys can form $MoPt_2$-type LRO below 863 K, but SRO measured above T_{tr} [22] resembles a concentration wave with $\boldsymbol{k} = (1\frac{1}{2}0)$, which is associated with distinct structures such as the Al_3Ti prototype.

2.4 Theoretical overview of $3d$ CCAs

The Cr-Ni system in fact appears to provide a template for the ordering of many fcc CCAs containing concentrated Cr, namely the derivatives of CrMnFeCoNi. These alloys consistently exhibit a $\sim$900 K phase transition that calorimetrically resembles the onset of $MoPt_2$-type $CrNi_2$ in Cr-Ni alloys [23]. Compositionally comparable CrCoNi is predicted to form a

Ref.	system	j	x_j	conditions	T (K)	T/T_{tr}	$\alpha_{ij}^{(1)}$	$\alpha_{jj}^{(1)}$
[16]	Cr-Ni	Cr	0.213	annealed 480 h	741	0.86	-0.1061	0.392
	Cr-Ni	Cr	0.201	annealed 320 h	828	0.96	-0.0990	0.394
	Cr-Ni	Cr	0.206	annealed 2.5 h	973	1.13	-0.0819	0.316
[17]	Cr-Ni	Cr	0.199	annealed 480 h	744	0.86	-0.1119	0.449
[22]	Cr-Ni	Cr	$\frac{1}{4}$	*in situ*	833	0.97	-0.0874	0.262
	Cr-Ni	Cr	$\frac{1}{4}$	*in situ*	993	1.15	-0.0674	0.202
	Cr-Ni	Cr	$\frac{1}{3}$	*in situ*	923	1.07	-0.0997	0.199
	Cr-Ni	Cr	$\frac{1}{3}$	*in situ*	1073	1.24	-0.080	0.160
	V-Ni	V	$\frac{1}{4}$	*in situ*	1373	1.04	-0.131	0.393
	V-Ni	V	$\frac{1}{3}$	*in situ*	1228	1.03	-0.1217	0.243
	V-Ni	V	$\frac{1}{3}$	*in situ*	1248	1.04	-0.1201	0.240
	V-Ni	V	$\frac{1}{3}$	*in situ*	1343	1.12	-0.1115	0.223
	V-Ni	V	$\frac{1}{3}$	*in situ*	1413	1.18	-0.1045	0.209
[15]	Cr-Fe-Ni	Cr	0.2085	annealed 10h	773		-0.148	0.091

Table 2.1: Nearest-neighbor WC parameters ($\alpha_{ij}^{(1)}$ and $\alpha_{jj}^{(1)}$) calculated from diffuse scattering experiments for $3d$ alloys containing x_j of "ordering element" $j = \text{Cr}, \text{V}$. Annealed samples were quenched after annealing at T, while *in situ* experiments were performed at T. T_{tr} represents the order-disorder transition temperature of the nearest stoichiometric ordering. For Refs. [15, 17], one value of $\alpha_{ij}^{(1)}$ was selected from several similar calculations. For Ref. [15], $\alpha_{ij}^{(1)}$ represents the dominant unlike-pair correlation, $\alpha_{\text{CrNi}}^{(1)}$.

similar phase with an effectively random Co-Ni solution in place of Ni [12, 24], while systems such as CrFeCoNi may prefer an $AlNi_3$-type ($L1_2$) Cr sublattice [11].

Both structures minimize Cr nearest neighbors, as may be largely explained by electrostatic interactions arising from charge transfer among electronegatively distinct elements, e.g. Cr to Ni [25–27]. Ch. 4 explores how first-principles calculations suggest that magnetic interactions can also affect chemical ordering [11, 28], although Ch. 5 shows that our understanding of the magnetism of Cr in concentrated fcc alloys is incomplete; either standard theory is incorrect or the presence of significant antiferromagnetic order has been overlooked.

Nonmagnetic V displays similar but stronger ordering tendencies, with VCoNi appearing to form $AlNi_3$-type LRO [29] that is consistent with theoretical predictions [30]. Mn is also understood to promote ordering in some conditions, although its behavior is comparatively less well studied. A CuAu-type ($L1_0$) MnNi phase is found among the decomposition of CrMnFeCoNi [31] and has been further examined in FeMnNi [32]; more complex orderings have also been theorized, though not experimentally validated, for Cr-Mn-Ni and Cr-Mn-Fe-Ni alloys [28]. Cu is expected to cluster in FeCoNiCu alloys [33], just as in Ni-Cu [34]. Chemically distinct elements, such as Al, may also more readily cluster or form LRO [10].

While some recently studied CCAs appear approximately pseudobinary, the underlying physics of chemical rearrangement may nonetheless differ from their binary counterparts. For instance, the ordering of CrCoNi closely resembles that of $CrNi_2$ with a ten percent higher transition temperature [23], but the magnitude of its theoretical ordering energy [12] is several times larger, implying significant entropic differences. Conversely, the calculations of Ref. [11] suggest that the formation of a Cr sublattice in CrFeCoNi is associated with a relatively minor entropy reduction given the configurational freedom of the remaining elements; some more systematic study of these effects could prove insightful.

Of course, all previously referenced predictions were made under the assumption of thermodynamic equilibrium and comparatively fewer studies have tackled the formidable problem of CCA kinetics. Perhaps most notably, Du *et al.* [24] explored the evolution of SRO in CrCoNi via the discrete hopping of vacancies in kinetic Monte Carlo simulations parameterized using a carefully developed interatomic potential. Although necessarily involving significant approximation, their calculations suggest that SRO will at least initially form far faster than typical quenching rates. As an alternative approach, simpler mean-field kinetic models [35] may also prove useful for many-component systems, provided relevant thermodynamic and mobility data are available.

2.5 Diffraction

Several decades ago, the SRO/C of single-crystal binary alloys was routinely characterized using the diffuse scattering of monochromatic X-rays or neutrons, that is the intensity in the Brillouin zone not due to the underlying lattice or multiple-scattering events. After accounting for contributions from static lattice displacements, the elastic intensity scattered at wave vector $\boldsymbol{k}$ can be related to the $Q_{ij}(\boldsymbol{k})$ described by Eq. (2.2) [7,36]. WC parameters $\alpha_{ij}^{(p)}$, and hence $\alpha_{jj}^{(p)}$, may be subsequently obtained.

Table 2.1 summarizes a number of historical measurements of SRO in Cr-Ni and V-Ni alloys subject to various thermal histories in terms of the nearest-neighbor WC parameter, $\alpha_{\mathrm{CrCr}}^{(1)}$ or $\alpha_{\mathrm{VV}}^{(1)}$. Many of the considered samples contained similar fractions of Cr or V as CCAs of current interest and, while entropic considerations may differ, the basic picture of ordering is expected to be similar. Long-term annealing below T_{tr} increases the degree of order, but, for a given composition, the difference between the least and most ordered measurements is less than that between the least order and complete disorder ($\alpha_{ij}^{(p)} = 0$). Additionally, many of the least ordered values were obtained at elevated temperatures and SRO may further develop during cooling. These results, which are comparable to those for other binary systems, clearly indicate that perfect atomic-scale randomness should never be assumed, even in quenched samples.

Unfortunately, interpreting diffuse scattering becomes rapidly more challenging with increasing compositional complexity, as the intensity measured in many-component alloys simultaneously represents all interspecies correlations. Specific Q_{ij} may nonetheless be extracted from multiple measurements obtained under distinct scattering conditions. For in-

stance, Cenedese *et al.* [15] characterized SRO in a concentrated Cr-Fe-Ni alloy by analyzing diffuse neutron scattering from three samples with varying isotopic content, as included in Table 2.1. This said, few comparable studies exist.

Distinct scattering measurements may also be obtained from "resonant" X-ray energies corresponding to the absorption edges of individual alloy elements [7]. In this manner, Schönfeld *et al.* [11] investigated the diffuse scattering of CrFeCoNi, providing perhaps the most complete characterization of SRO in a CCA since the popularization of high-entropy alloys. While not determining specific pair correlations, they used complementary electronic structure calculations to deduce the partial formation of an $AlNi_3$-type ($L1_2$) Cr sublattice in a sample aged at approximately $0.8\,T_{\mathrm{tr}}$. Comparable data are not available for differently processed samples—in fact, I am aware of no other experiment of this type.

Many recent studies have instead favored TEM, which is discussed in Ch. 3. While various other phenomena can cause extra reflections that have been widely interpreted as ordering, the electron scattering contrast among $3d$ elements appears insufficient to detect SRO in many systems of interest [2, 19]. (Clustering, LRO, and even SRO involving distinct chemical species, such as Al or Pd in a $3d$ alloy, may be more readily visible.)

Most remaining evidence for SRO in CCAs is thus indirect, as is examined in Ch. 4. Some spectroscopy appears to support the presence of ordering [37–39], although these measurements may vary extremely subtly with SRO and also require comparison with simulated configurations, the accuracy of which has been questioned [40]. As another approach, atom-probe tomography may qualitatively reveal real-space concentration waves along one sample dimension [18].

Chapter 3

Reinterpreting electron diffraction

Historically established methods for measuring chemical SRO were briefly discussed in Ch. 2, but most recent attempts to characterize the phenomenon have instead favored TEM-based techniques that do not require a beamline facility or single-crystal samples. In electron diffraction patterns obtained from a variety of fcc CCAs, diffuse intensities at superlattice positions have been widely, though not universally, attributed to the presence of local order. Many of these samples were subject to minimal thermal processing beyond high-temperature homogenization, seemingly supporting the argument that ångström-scale order could play an important role in a wide range of properties.

Perhaps most prominently, the observation of SRO in VCoNi was proposed [29] on the basis of diffuse intensities at $\frac{1}{2}\{311\}$ superlattice sites in reciprocal space while imaging in the $[\bar{1}12]$ zone axis (ZA), which indicates the crystallographic direction of electron incidence. An equivalent electron diffraction pattern is shown in Fig. 3.1. Additional $\frac{1}{3}\{422\}$ intensities were later reported in the $[\bar{1}11]$ ZA [42]. Similar observations have been at various points attribtued to SRO in CrCoNi [41, 43], CrMnFeCoNi [44], VFeCoNi [45], a Cr-Ni-based alloy [46], and Mn-Fe-based alloys [47–50], The same features have also been reported without the assumption of SRO [19, 51–54].

Some of these reflections are consistent with the partial formation of a CuPt-type ($L1_1$) concentration wave involving the compositional enrichment and depletion of alternating {111} (and simultaneously {311}) planes, as illustrated in Fig. 3.2(a). Diffuse intensities in VCoNi and CrCoNi have been interpreted to reflect modulations of V or Cr concentrations in this manner [29, 42, 43], largely on the basis of electronic structure calculations indicating repulsive interactions between V-V and Cr-Cr neighbors, although CuPt-type ordering has the same nearest-neighbor pair frequencies as a random alloy. Some effort has been made to support this theory with atomic-scale composition mapping [29, 43, 45], but, in contrast to the diffuse intensities themselves, these measurements are noisy and susceptible to local fluctuations, making it difficult to draw statistical conclusions.

Regardless of chemical specifics, the presence of superlattice reflections should not be regarded as incontrovertible evidence for ordering. In fact, widespread interpretations of SRO are questionable on several accounts, such as the absence of additional expected peaks.

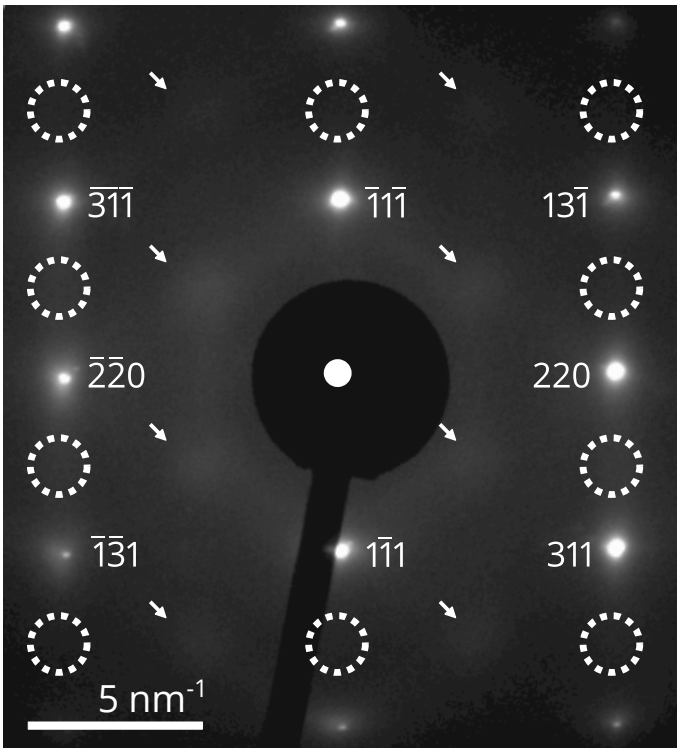

Figure 3.1: Electron diffraction of CrCoNi in the $[\bar{1}12]$ ZA. This pattern, which is based on experimental data from a previous study [41], is representative of literature results for alloys discussed in the text. Diffuse intensities at $\frac{1}{2}\{311\}$ superlattice positions are marked with arrows, but there are no peaks at $\frac{1}{2}\{111\}$ sites, as highlighted by the dotted circles.

By the symmetry of the fcc lattice, a CuPt-type decoration can equivalently occur in four rotational variants, corresponding to order on the $(\bar{1}11)$, (111), $(11\bar{1})$, or $(1\bar{1}1)$ planes, with four additional antiphase structures that are redundant for purposes of diffraction. The four rotational variants are illustrated in the top row of Fig. 3.3 from the perspective of the $[\bar{1}12]$ ZA, with atomic columns shaded by composition; the reciprocal-space intensities expected from each variant are shown below for the same ZA. (Reflections were determined from the basic diffraction criterion for concentration waves [8], as restricted by the two-dimensional nature of TEM, and verified through simulations.)

As illustrated in Fig. 3.3(a), the $\frac{1}{2}\{311\}$ peaks visible in Fig. 3.1 are associated only with the $(\bar{1}11)$ variant. While the variants on the (111) and $(11\bar{1})$ planes are not expected to produce additional reflections in this orientation, the $(1\bar{1}1)$-based variant depicted in Fig. 3.3(d) should be readily visible, as it would involve composition modulation across the $(1\bar{1}1)$ planes that form the rows of atomic columns viewed in TEM. Nonetheless, the associated $\frac{1}{2}(1\bar{1}1)$ peaks are missing from all experimental characterizations of the $[\bar{1}12]$ ZA, through either electron diffraction or the Fourier transformation of dark-field images [19, 29, 41–52].

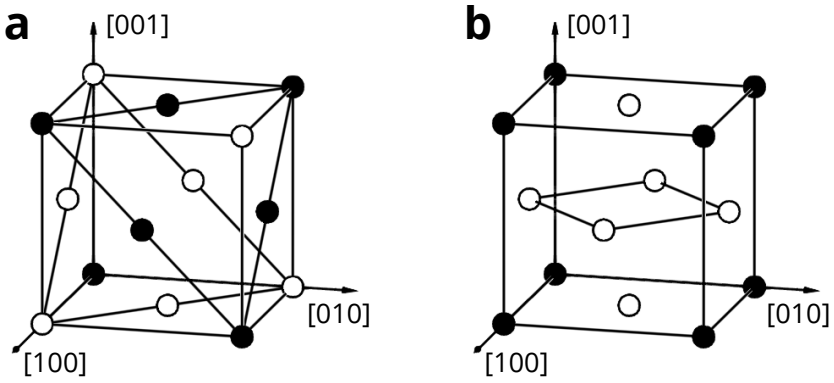

Figure 3.2: Schematics of CuPt- and $AlNi_3$-type orderings. (a) The CuPt-type ($L1_1$) decoration of an fcc lattice. SRO based on this structure has been proposed for VCoNi and CrCoNi with V or Cr-rich • sites and complementarily depleted ∘ sites on alternating (111) planes. (b) Similarly, an $AlNi_3$-type ($L1_2$) unit cell. First-principles calculations suggest that this general form of ordering, in which V or Cr-rich • sites form a sublattice that minimizes nearest neighbors, should be far more energetically favorable [24], if not the ground state [11, 30], in these systems.

Locations where additional reflections would be expected are circled in Fig. 3.1 and marked in Fig. 3.3(d). Given the quantity of material sampled across numerous studies, the absence of a variant is not statistically conceivable.

One could attempt to construct an alternative structure giving rise to only $\frac{1}{2}\{311\}$ intensities, but every $\frac{1}{2}\{311\}$ peak is related to a $\frac{1}{2}\{111\}$ spot by a $\{200\}$ reciprocal lattice vector, e.g. $\frac{1}{2}(131) - (020) = \frac{1}{2}(1\bar{1}1)$, as is the case of Fig. 3.3(d). Since the diffraction criterion for concentration waves is independent of reciprocal lattice translations [8], any ordering that produces $\frac{1}{2}\{311\}$ peaks should also effect $\frac{1}{2}\{111\}$ intensities as long as all variants are present.

Furthermore, $\frac{1}{3}\{422\}$ and $\frac{1}{2}\{311\}$ reflections have very recently been reported in pure Cu [19]; $\frac{1}{3}\{422\}$ reflections were also previously observed in pure Ni [52]. Evidently, superlattice intensities in pure elements cannot represent chemical ordering and require another explanation, of which there are in fact several.

One is the presence of nanoscale planar defects. Forbidden reflections expected from stacking faults or nanotwins in an fcc lattice [55] are listed in Table 3.1. Remarkably, these are the exact features that have been reported in the [011], [$\bar{1}$12], [$\bar{1}$11], and [013] ZAs of concentrated alloys, offering an alternative explanation for the experimental findings described above. As structural defects break the symmetry of the reciprocal lattice, it is possible for $\frac{1}{2}\{311\}$ peaks to appear without $\frac{1}{2}\{111\}$ counterparts. Of course, the obvious objection to this hypothesis is that most imaged samples appeared to contain no such imperfections in the examined regions. Considering that stacking faults and related structures are usu-

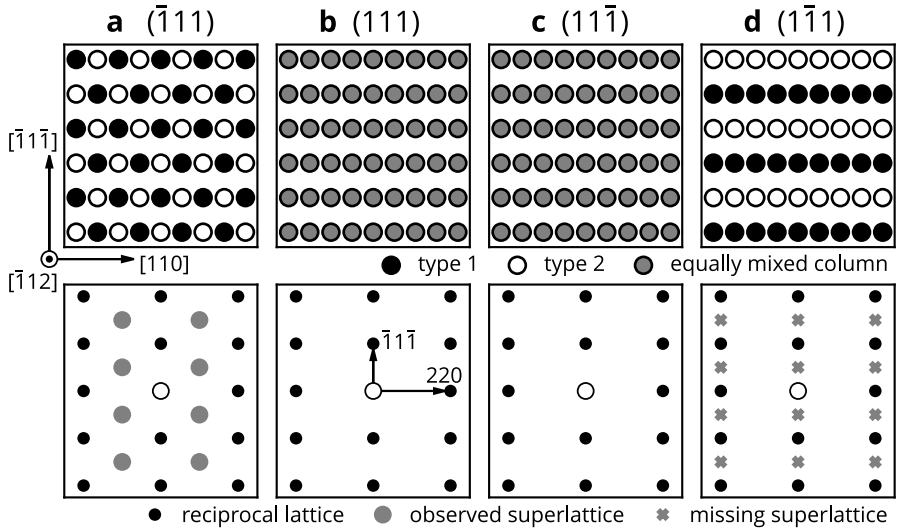

Figure 3.3: Diffraction of CuPt-type ordering in the [$\bar{1}$12] ZA. (a-d) The four rotational variants of a CuPt-type structure, consisting of ordering on the denoted planes. In the top row, structures are drawn from the perspective of the [$\bar{1}$12] ZA, with columns of atoms shaded according to the average composition. (In CuPt, types 1 and 2 would represent Cu and Pt; in recently proposed SRO, they correspond to Cr or V enrichment and depletion as in Fig. 3.2.) The reciprocal-space signatures of the four variants are shown below for the same ZA. Only reflections associated with variant (a) have been reported in the discussed alloys, questioning the existence of this form of order.

Table 3.1: Extra reflections from fcc planar defects. The reciprocal-space features expected from planar defects [55] match recent experimental observations in concentrated alloys, as noted for each ZA. In most cases, the intensities were originally attributed to SRO.

ZA	Extra reflections	Observations
[011]	streaking	[46, 50, 51, 56]
[$\bar{1}$11]	$\frac{1}{3}${422}	[19, 42, 46, 49, 51–54]
[$\bar{1}$12]	$\frac{1}{2}${311}	[19, 29, 41–52]
[013]	$\frac{1}{2}${311}	[49, 52]

ally quite visible under TEM, some explanation of how presumably nanoscale planar defects could otherwise escape detection would be required to prove their generation of the discussed features.

While clearly visible stacking faults produce sharp superlattice reflections [55], the diffuseness of the discussed intensities could imply the presence of smaller, less readily detected defects, just as SRO causes faint reflections compared to the sharp superlattice peaks resulting from long-range order (LRO). Both faulted (Frank) loops and stacking fault tetrahedra should produce the extra reflections listed in Table 3.1 and, if small enough, could plausibly escape direct recognition. In many recent studies, superlattice intensities have been associated with tiny localized features, which could correspond to defect structures. Moreover, two recent investigations have connected the enhancement of diffuse intensities to mechanical deformation [50] and irradiation [44], while brighter reflections have been found near a crack tip [46]. Both deformation and irradiation are well known to induce planar defects at the expense of chemical order, supporting this hypothesis—in fact, the intensity of some peaks has been directly correlated the density of planar defects [50].

Most observations in the [011] ZA support the absence of detectable SRO—CuPt-type ordering should produce additional superlattice reflections in this ZA, which are generally not observed [29, 43, 56]. (Faint intensities at $\frac{1}{2}\{111\}$ positions were suggested by Ref. [42], but the signal in this region seems comparable to the background noise level. Clearer $\frac{1}{2}\{111\}$ intensities in the [011] ZA have been proposed following the application of a novel post processing algorithm [57], although this technique may require further discussion of a technical nature beyond the scope of this chapter.) Several studies have instead reported streaking in this ZA [46, 50, 51, 56], which would also be consistent with planar defects [55]. Others have found no extra features, but the absence of observation in specific instances would hardly be surprising given variation in sample preparation and the inherently local nature of the proposed defects.

Another theory is that the extra reflections are merely artifacts caused by "relrod spiking" from higher-order Laue zone (HOLZ) diffraction [19], which could in principle account for the locations of most reported peaks, although the HOLZ intensities predicted by kinematical theory are negligible [52]. While dynamical scattering could theoretically contribute to forbidden reflections, it is not immediately clear how this would occur in the sample geometries used in the literature, which were too thin to even produce Kikuchi diffraction. Streaking in the [011] ZA [46, 50, 51, 56] and the specific peaks observed in the [013] ZA [49, 52] may also be more consistent with faulting [55].

It has been additionally suggested that surface steps could produce the extra reflections [19, 52], as has been demonstrated for $\frac{1}{3}\{422\}$ intensities in the $[\bar{1}11]$ ZA [58]. However, it is less clear if this mechanism is consistent with observations in other ZAs. Additionally, surface-step reflections have been primarily observed in deposited thin films with clear step contours, which are not apparent in recent observations of differently processed samples.

Somewhat before recent interest, $\frac{1}{2}\{311\}$ reflections in the $[\bar{1}12]$ ZA of an $Al_{0.5}CrFeCoNiCu$ alloy were suggested to possibly originate from thermal diffuse scattering [51]. However, it has also been shown that at least $\frac{1}{3}\{422\}$ reflections remain essentially unchanged at liquid

nitrogen temperatures [52]. Alternatively, scattering from static lattice displacements has been proposed as another potential source of extra intensities [53,54]. This phenomenon can break the symmetry of the reciprocal lattice [59], although a specific mechanism by which it could produce the discussed observations has not been established. Like SRO, static displacement scattering also could not explain the intensities observed in pure elements.

While the connection between the extra reflections and SRO is questionable on a purely experimental basis, the proposed structures are also largely inconsistent with the bonding principles predicted by standard density-functional theory, either directly or through parameterized interatomic potentials. As previously noted [24, 43], CuPt-type ordering is clearly energetically unfavorable in otherwise similar V-Ni and Cr-Ni alloys. In these systems, experimental SRO has been primarily interpreted in terms of $AlNi_3$-type ($L1_2$, see Fig. 3.2) or Al_3Ti-type (DO_{22}) concentration waves [16, 17, 22, 60], both of which minimize nearest neighbors among the ordering solute.

First-principles calculations consistently indicate that VCoNi and CrCoNi should order similarly to the aforementioned binaries, with VCoNi clearly favoring an $AlNi_3$-type V sublattice [30] and similar, though not identical, preferences noted for CrCoNi [3, 12, 24]. While SRO may differ from the LRO ground state [8], the underlying interactions are expected to be comparable and there is essentially no indication of any energetic driving force for the formation of CuPt-type ordering.

In practice, the basic predictions of electronic structure calculations are largely supported by diffuse X-ray scattering in CrFeCoNi, which reveals an incipient $AlNi_3$-type Cr sublattice [11] after long-term aging below the order-disorder transition temperature. Moreover, VCoNi alloys readily form fully ordered $AlNi_3$-type domains (see Fig. 3.2), which were observed alongside the nominally disordered regions characterized by Ref. [29]. It would be unexpected for this material to host SRO corresponding to an unrelated structure immediately adjacent to the theoretically predicted LRO.

A few studies have nonetheless tried to reconcile experimental observations with theoretical predictions. In particular, local instances of ordering on $\frac{1}{2}\{311\}$ planes were identified in high-temperature thermodynamic simulations of CrCoNi parameterized by a carefully developed "neural network" interatomic potential [24]. However, the CuPt-type structure was noted to be energetically unfavorable and it is unclear if these regions represent anything beyond random fluctuations. Their equilibrium frequency does not vary with temperature above the order-disorder transition and equivalent instances of theoretically favorable {100} and {110}-based motifs are consistently more prevalent, even though their associated peaks are not found experimentally.

Clearer agreement has been found between experimental diffraction patterns and simulations [57] for certain previously generated theoretical structures [3]. These, however, were selected from a large collection of tiny configurations that were created to statistically explore highly speculative ordering principles rather than represent realistic chemical environments. Consequently, individual structures likely contained configurational fluctuations that, given the small cell size, could lead to various extra reflections.

Altogether, there seems to be little theoretical basis for any form of SRO consistent with

the electron diffraction of VCoNi, CrCoNi, and other similar alloys, while reported features consistently match those expected from symmetry-breaking effects such as changes in the stacking sequence. This is not to say that any experimental sample necessarily lacked SRO, simply that it may not be definitively detected by the employed techniques.

Chapter 4

Chemical and magnetic order in CrCoNi

4.1 Introduction

As seen in Ch. 3, the SRO of CrCoNi has received particular attention in the study of ordering in $3d$ CCAs. This alloy is considered a model system and is noteworthy for its cryogenic damage tolerance and general mechanical superiority to the five-component CrMnFeCoNi [61–63]. Theoretical aspects of ordering in this system were briefly mentioned in Chs. 2 & 3, but the previously discussed experimental situation motivates a closer examination of simulation results.

Chemical SRO in CrCoNi was theoretically first examined by Tamm *et al.* [64] through Monte Carlo (MC) optimization of on-lattice density-functional theory (DFT) simulations; similar calculations were later performed by Ding *et al.* [65]. The results of both studies are summarized in Table 4.1 in terms of nearest-neighbor Warren-Cowley (WC) SRO parameters [36] (see Eq. (2.1)). Although extremely limited in statistical sampling, these computations suggest a general trend of additional Cr-Co and Cr-Ni neighbors at the expense of Cr-Cr pairs that is qualitatively supported by analysis of X-ray absorption fine structure [66]. SRO of this form has been predicted to appreciably affect properties ranging from magnetic moment [64] to stacking-fault energy [65], but the nature of the more than 40 meV per atom driving force (i.e., reduction in energy) observed in MC simulations had not been thoroughly explained.

In this chapter, further application of spin-polarized DFT reveals how the dominant bonding preferences of the CrCoNi system are, at least in ground state electronic structure calculations, closely coupled to magnetic interactions. Chief among these is the frustration of antiferromagnetic Cr, which can be greatly relieved by the minimization of Cr-Cr nearest neighbors. Indeed, the frequency of these bonds is shown to fully account for the energies of structures containing previously reported nearest-neighbor ordering. Calculations further indicate that magnetically aligned, but not magnetically opposed, Co-Cr pairs are also

repulsive.

This result is, especially in retrospect, quite surprising, given the uncertain nature of magnetic order in the system. While some related alloys possess ferromagnetic ground states that disorder well below ambient temperature [67], no such transition has been reported in CrCoNi. Like the Cr-Ni alloys considered in Ch. 5, CrCoNi is often considered paramagnetic, although paramagnetism, while possibly arising from longitudinal spin fluctuations, is not an electronic ground state. Standard theory predicts that random solutions of CrCoNi are ferromagnetic at 0 K, but spontaneous moment is generally not observed, at least above 5 K [68]. Some have consequently assumed that the system magnetically disorders at lower temperatures [12, 67], but this resolution is hardly satisfactory from a theoretical perspective, as the calculated magnetic energies would imply a much higher magnetic order-disorder transition temperature. As more rigorously examined in Ch. 5, it is entirely possible that the employed theory, which is described in detail in Ref. [3], is simply inaccurate, although this would represent a rather spectacular failure of methods that otherwise seem to satisfactorily describe the magnetism of $3d$ transition metal alloys. In light of this situation, considering a role for magnetism in the ordering of this system is extremely speculative, perhaps irresponsibly so, but given the findings of Ch. 5, I do not think immediately dismissable.

This line of analysis was originally inspired by some comments made in prior works, e.g., Tamm *et al.* [64] raised the possibility of magnetic frustration in CrCoNi. A role for magnetism had also been previously proposed in a CrFeCoNi alloy, in which the antiferromagnetism of Cr was attributed to the promotion of a CuPt-type Cr sublattice, as possible given $x_{\mathrm{Cr}} = 0.25$ [69]. In this chapter, CrCoNi is found to favor a reminiscent sublattice of magnetically aligned second-nearest neighbor Cr atoms. While all these studies have similarly relied on ground state electronic structure calculations, simulations assuming paramagnetism via the disordered local moment approximation consistently underestimate the experimental order-disorder transition temperature, whereas higher degrees of magnetic order significantly improve predictions [11]. It thus does not seem entirely unreasonable to consider a role for at least *magnetic* short-range order, which, as discussed in Ch. 6, is a generally underappreciated phenomenon in pure elements, to say nothing of many-component alloys.

While these observations do not directly address thermodynamic aspects of chemical or magnetic order, classical simulations using cluster expansions [70] and the embedded-atom method [71] had suggested that significant degrees of SRO may exist even at high temperatures. However, although some progress has been made since this work was performed [24], the kinetics of the system remain largely uncertain. Yin *et al.* [40] questioned the impact or even existence of SRO in these materials, suggesting that the DFT calculations supporting its existence may be erroneous. Indeed, computational predictions for random solid solutions of CrCoNi notably contradict experimental measurements of spontaneous magnetization [68,72] and partial molar volumes [40] in ostensibly disordered samples. Addressing these apparent anomalies, the previously identified ordering principles are applied to nonstoichiometric Cr-Co-Ni compositions in order to replicate the scenarios studied by Refs. [40,68]. The inclusion of SRO in DFT calculations is shown to, at least in principle, theoretically reproduce exper-

Table 4.1: WC SRO parameters (Eq. (2.1)) reported by two previous DFT-MC studies (second and third columns), compared to a simple structural model (fourth column)

Neighbor Pair	Tamm *et al.* [64] DFT-MC 500 K	Ding *et al.* [65] DFT-MC 500 K	Simple structural model
Cr-Cr	0.42	0.40	α_{CrCr}
Co-Cr	-0.16	-0.25	$-\alpha_{\mathrm{CrCr}}/2$
Ni-Cr	-0.27	-0.15	$-\alpha_{\mathrm{CrCr}}/2$
Ni-Co	0.15	0.19	$\alpha_{\mathrm{CrCr}}/2$
Co-Co	0.01	0.06	0.0
Ni-Ni	0.12	-0.04	0.0

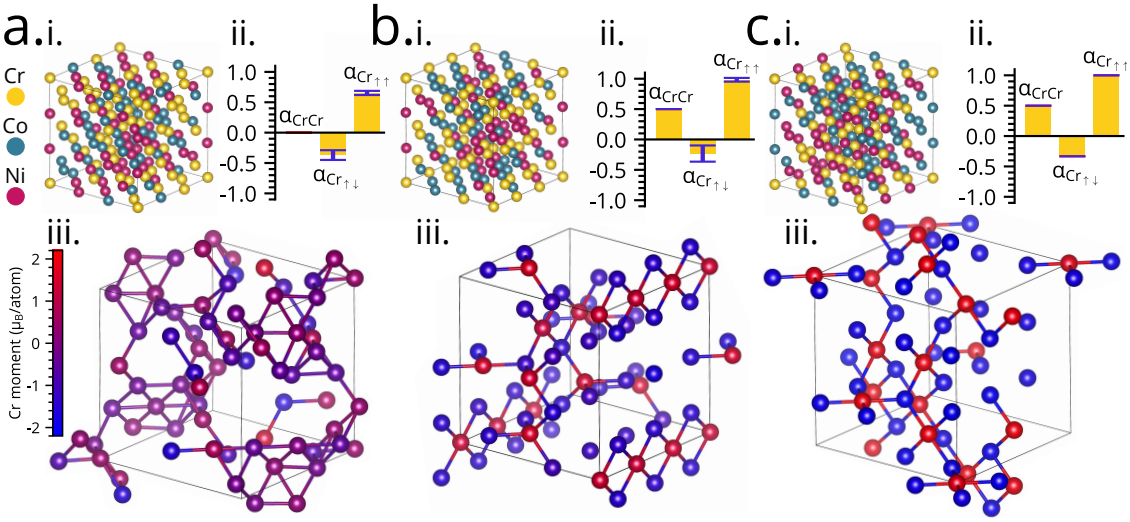

Figure 4.1: An analysis of apparent magnetic frustration in (a) quasirandom, (b) Cr-Cr neighbor-minimized ($\alpha_{\mathrm{CrCr}} = 0.5$ in the simple structural model), and (c) "spin-ordered" CrCoNi. For each ordering model, (i) an example simulation cell is shown alongside (ii) WC values (Eq. (2.1)) for chemical (α_{CrCr}), opposite-spin ($\alpha_{\mathrm{Cr}_{\uparrow\downarrow}}$), and same-spin ($\alpha_{\mathrm{Cr}_{\uparrow\uparrow}}$) Cr pairs. In (iii), the Cr atoms from (i) are colored by magnetic moment, with nearest-neighbor Cr-Cr bonds drawn. Error bars indicate SD from 20 configurations.

imental measurements, offering the possibility that previously examined material contained significant degrees of order. This interpretation suggests that SRO is not only critical for a wide range of properties, but also is widely prevalent under standard processing conditions.

4.2 Results

The magnetic exchange interactions of disordered CrCoNi appear highly frustrated, as exemplified by the quasirandom [73] configuration depicted in Fig. 4.1(a)(i). This said, the traditional notion of frustration, as pioneered in highly localized magnets, may be less straightforward in metals such as Ni or Cr in which magnetism is highly itinerant, practically meaning that the formation of local moment is inherently unfavorable and stabilized only by energy reductions caused by exchange interactions. The fundamental itineracy of magnetism in transition metal alloys is further discussed in Ch. 5. For the supercell depicted in Fig. 4.1(a)(i), panel (iii) shows the local magnetic moments of Cr atoms calculated using spin-polarized DFT, with nearest-neighbor Cr-Cr bonds identified. Frustration appears to suppress the local moments of Cr atoms that are bonded to several other Cr nearest neighbors. In contrast, Cr atoms with fewer Cr neighbors resolve into a network of alternating spins. Simplistically assigning Cr atoms "up" and "down" states from the sign of their local moment enables the calculation of magnetic WC values (Eq. (2.1)), as described in Ref. [3]. Considering 20 quasirandom configurations, the WC value for same-spin Cr (denoted $\alpha_{\mathrm{Cr}_{\uparrow\uparrow}}$) is 0.65 ± 0.04, while opposite-spin pairs are commensurately more likely with $\alpha_{\mathrm{Cr}_{\uparrow\downarrow}} = -0.37 \pm 0.08$, as graphed in Fig. 4.1(a)(ii). Although not accounting for moment magnitudes, these numbers highlight the unfavorability of magnetically aligned Cr pairs.

In a ternary fcc solid solution of equimolar composition, local chemical ordering can reduce the mean number of same-species nearest neighbors to as low as two ($\alpha_{\mathrm{CrCr}} = 0.5$), offering significant relief from frustration. In what follows, the effect of Cr neighbor reduction is studied through supercells following a simple structural model in which α_{CrCr} is the dominant ordering term and other values are nonzero only by conservation of probability (see the fourth column of Table 4.1).

Energy and magnetization for configurations with $\alpha_{\mathrm{CrCr}} = 0.3, 0.4, 0.45, 0.5$ (plus the quasirandom case of $\alpha_{\mathrm{CrCr}} = 0$) are plotted in Fig. 4.2, alongside those of supercells matching the nearest-neighbor WC parameters of Tamm *et al.* [64] and Ding *et al.* [65] reproduced in Table 4.1. It should be emphasized that these are not exact replicas of those studies' configurations; Tamm *et al.* [64] report a formation energy of 43.7 meV per atom, substantially lower than the 62.2 ± 2.7 meV per atom recalculated presently. Nevertheless, the results displayed in Fig. 4.2 indicate that, within the margin of error, the energy and magnetization of all these configurations closely follow α_{CrCr} and that other chemical ordering terms, insofar as they are represented by nearest-neighbor WC parameters, are much less energetically relevant. In the extreme case of $\alpha_{\mathrm{CrCr}} = 0.5$, formation energy and net moment are 52.0 ± 3.5 meV per atom and 0.054 ± 0.04 μ_{B} per atom, respectively, reduced from 88.0 ± 3.3 meV per atom and 0.28 ± 0.04 μ_{B} per atom for a quasirandom solution.

Accounting for higher-order effects

The discrepancy between the formation energy determined by Tamm *et al.* [64] and the value recalculated on the basis of their reported WC parameters suggests the existence of

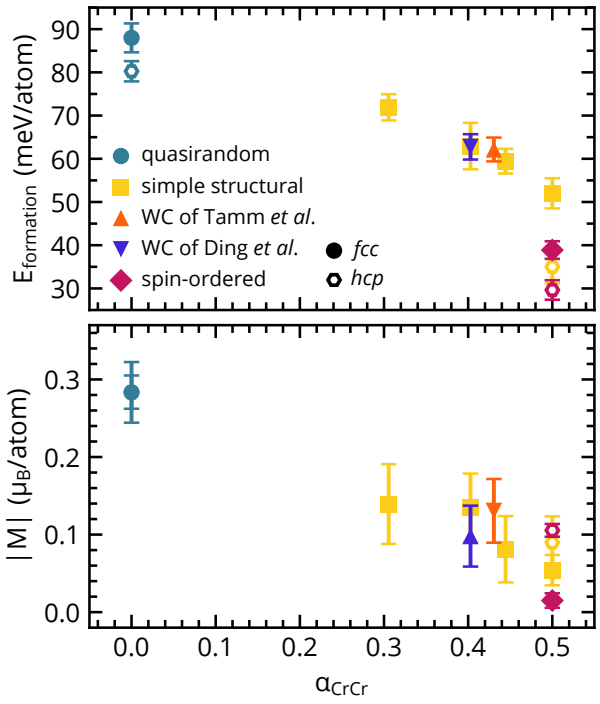

Figure 4.2: Formation energy and magnetization for various models of SRO in CrCoNi as a function of the Cr-Cr nearest-neighbor WC SRO parameter (Eq. (2.1)). Hollow hexagonal markers represent the model of the corresponding color applied to hcp lattices. Each datum is the average of 20 configurations; error bars indicate SD.

order beyond what can be understood in terms of chemical nearest neighbors. Furthermore, the range of Co and Cr atomic moments obtained under the simple structural model for $\alpha_{\mathrm{CrCr}} = 0.5$, presented in Fig. 4.3, indicates that some degree of frustration persists in this regime. Comparing these values to the moments of neighboring elements reveals trends that offer clues to the underlying magnetic interactions.

Specifically, Fig. 4.3 shows how Co atoms favor moments antiparallel to those of immediately adjacent Cr. While Ni atoms possess negligible local moment under all degrees of order, most Co align ferromagnetically, the direction of which will define a reference spin "up" state, to which Cr atoms are either aligned ($\mathrm{Cr}_\uparrow$) or opposed ($\mathrm{Cr}_\downarrow$). The preferred antialignment of Cr and Co moments is reflected in Figs. 4.1 and 4.3 (as well as Tamm *et al.* [64]), where $\mathrm{Cr}_\downarrow$ outnumber $\mathrm{Cr}_\uparrow$ by a factor of three. Of course, the presence of $\mathrm{Cr}_\uparrow$ is required to minimize the possibility of like-spin Cr pairs; $x_{\mathrm{Cr}_\downarrow} = \frac{1}{4}$ is the maximum possible concentration that can exist on an fcc lattice without same-species nearest neighbors. Consequently, the minimum fraction of $\mathrm{Cr}_\uparrow$ is $x_{\mathrm{Cr}_\uparrow} = x_{\mathrm{Cr}} - x_{\mathrm{Cr}_\downarrow} = \frac{1}{12}$.

The magnitude of a $\mathrm{Cr}_\downarrow$ moment most strongly depends on none of its nearest neighbors,

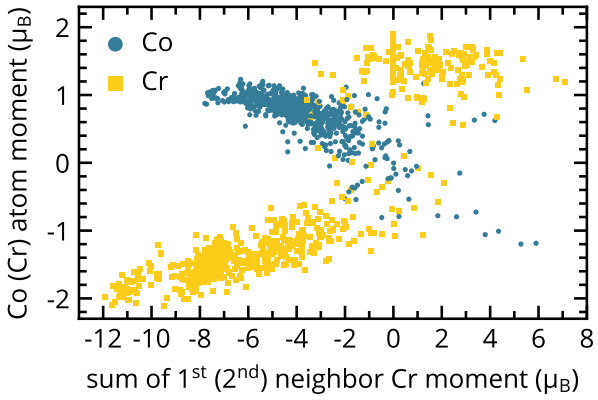

Figure 4.3: Atomic moments of Co and Cr atoms from 20 configurations minimizing adjacent Cr in the simple structural model ($\alpha_{\mathrm{CrCr}} = 0.5$). Co and Cr moments are plotted against the cumulative moments of their nearest-neighbor and second-nearest-neighbor Cr atoms, respectively.

but rather the magnetization of its Cr second-nearest neighbors, as plotted in Fig. 4.3. In particular, these data indicate that second-nearest-neighbor sublattices of $\mathrm{Cr}_{\downarrow}$ (i.e., $\mathrm{Cr}_{\downarrow}$ with six $\mathrm{Cr}_{\downarrow}$ second-nearest neighbors) consistently display local moments in the vicinity of -2 μ_{B}.

These preferences motivate a new "spin-ordered" model that reduces $\mathrm{Cr}_{\uparrow}$-$\mathrm{Cr}_{\uparrow}$, $\mathrm{Cr}_{\downarrow}$-$\mathrm{Cr}_{\downarrow}$, and Co-$\mathrm{Cr}_{\uparrow}$ nearest neighbors while maximizing $\mathrm{Cr}_{\downarrow}$-$\mathrm{Cr}_{\downarrow}$ second-nearest neighbors (see Ref. [3] for a full description). The average formation energy and net moment for 20 of these supercells are 38.9 ± 2.0 meV per atom and 0.015 ± 0.01 μ_{B} per atom, respectively. These values, included in Fig. 4.2, are not only substantially lower than in the simple structural model, but also display minimal spread, implying that the remaining configurational degrees of freedom are not energetically significant.

Interestingly, both models of SRO appear similarly applicable to hexagonal close-packed (hcp) lattices, which 0 K DFT predicts to be lower in energy under all degrees of order. This trend can be seen in Fig. 4.2, which includes the formation energy of quasirandom, $\alpha_{\mathrm{CrCr}} = 0.5$, and spin-ordered hcp configurations at 80.3 ± 2.3, 35.0 ± 3.7, and 29.6 ± 2.3 meV per atom, respectively. These values are all below those of the corresponding fcc structures, by a margin ranging from 7.7 meV per atom in the quasirandom case to 17.0 meV per atom for the simple structural model. The net magnetizations of hcp configurations containing SRO, however, are higher than their fcc counterparts as the local moments of hcp $\mathrm{Cr}_{\downarrow}$ atoms do not realize the same magnitudes, especially in the spin-ordered structures. In fact, the relatively small energy difference between simple structural and spin-ordered hcp models suggests that the latter's non-$\mathrm{L1}_2$ sublattice lacks the effect of its fcc counterpart.

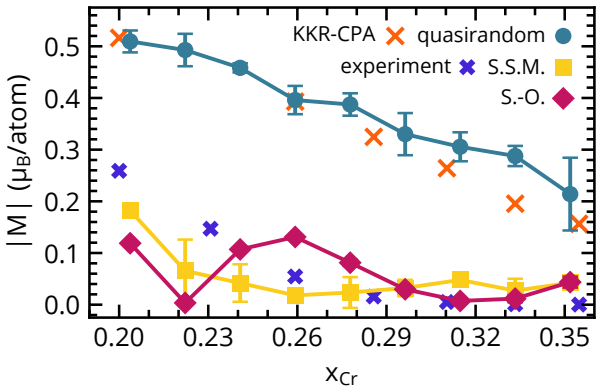

Figure 4.4: Zero-field and temperature magnetization calculated under several different ordering models for a range of x_{Cr}, where $x_{\mathrm{Co}} = x_{\mathrm{Ni}} = (1 - x_{\mathrm{Cr}})/2$, compared to 5-K experimental measurements from Ref. [68]. "S.S.M." and "S.-O." indicate the ($\alpha_{\mathrm{CrCr}} = 0.5$) simple structural and spin-ordered models, respectively. Data points average five configurations, except the equimolar composition, which uses data from Fig. 4.2. Error bars indicate SD.

Reproducing magnetization measurements

Chemical and magnetic ordering phenomena have been shown to reduce formation energy, but their realization in real samples of CrCoNi is not well understood. Indeed, SRO originates from a multitude of thermodynamic and kinetic factors competing throughout a sample's thermal history, which are extremely challenging to model collectively. Given the comparable level of difficulty faced in the experimental characterization of SRO among these elements, considering indirect evidence for its presence can prove insightful. In what follows, simulations of structures containing varying degrees of configurational and magnetic order, as described above, provide a potential resolution to discrepancies between magnetization and volume measurements at odds with DFT predictions for random alloys.

One such anomaly was found by Sales *et al.* [68, 72], in which spontaneous magnetization was measured at 5 K for samples of fcc $\mathrm{Cr}_x\mathrm{Co}_{(1-x)/2}\mathrm{Ni}_{(1-x)/2}$ with $0.2 \leq x \leq 0.355$. Anomalous magnetic measurements has been connected to local chemical rearrangement for decades; e.g., Ref. [74] inferred the presence of clustering in Ni-Cu alloys using a simple analytical model of local moments depending on neighbor frequencies. In the low-temperature limit, experimental magnetization is generally comparable to the predictions of electronic structure calculations, which quantitatively describe the magnetic ground states of many alloys such as FeCoNi [67], which is not known to host significant SRO/C.

Experimental values for CrCoNi from Ref. [68] are reproduced in Fig. 4.4, alongside computational results they obtained using the multiple-scattering method of Korringa, Kohn, and Rostocker (KKR) with the coherent-potential approximation (CPA) [75], which assumes complete compositional disorder. The KKR-CPA results agree well with present calculations

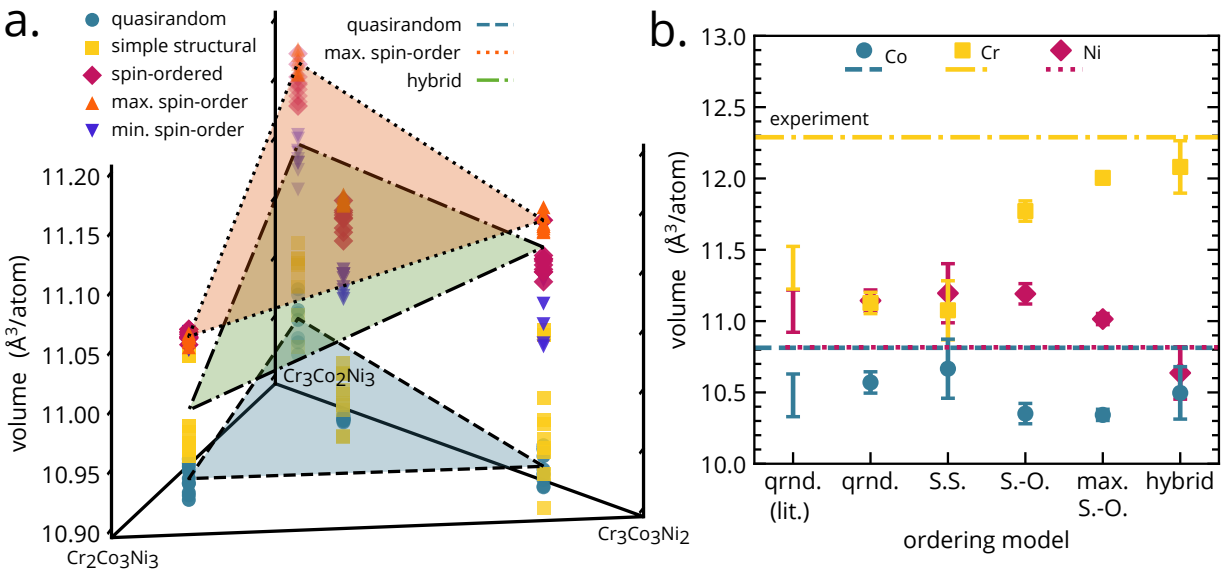

Figure 4.5: (a) Total alloy volume (per atom) for several ordering models applied to CrCoNi, $Cr_{10}Co_{13}Ni_{13}$, $Cr_{13}Co_{10}Ni_{13}$, and $Cr_{13}Co_{13}Ni_{10}$, following Ref. [40]. Planes illustrate fits of Eq. (4.1) to various models. (b) Partial molar volumes regressed from ordering models shown in (a) or a combination thereof, compared to the experiments of Ref. [40]. "qrnd." refers to quasirandom configurations, "S.S.M." stands for the ($\alpha_{\mathrm{CrCr}} = 0.5$) simple structural model, and "S.-O." denotes spin-ordered. "min." and "max." respectively indicate minimum and maximum. The "hybrid" model considers different ordering models at compositions based on previous results. As in Ref. [40], error bars indicate the 95% CI.

for quasirandom configurations, as shown in Fig. 4.4, but both methods predict magnetizations significantly larger than experimental measurements.

Two further sets of simulation results, each representing a different model of SRO, are included in Fig. 4.4. The first dataset (gold squares) applies the simple structural model of maximally eliminating Cr nearest neighbors to additional compositions. In a similar manner, the second approach (magenta diamonds) uses the chemical and magnetic principles of the spin-ordered state. Interestingly, the spin-ordered model appears slightly closer to experiment around the equimolar composition, the simple structural model's trend better describes the behavior of lower Cr concentrations. The difference, however, is fairly small and certainly within the overall margin of error. Still, the possibility that distinct compositions could lead to different degrees of order is crucial for the next set of calculations, in which measurements concerning partial molar volumes are analogously reproduced using SRO.

Reproducing volume measurements

In order to assess lattice misfit and predict yield strength, Yin *et al.* [40] regressed partial molar volumes of individual chemical species (V_{Cr}, V_{Co}, and V_{Ni}) from the measured total volume (V_{alloy}) of several samples in close compositional proximity. Specifically, they determined V_{Cr}, V_{Co}, and V_{Ni} from four measurements of V_{alloy} by fitting to the relation

$$V_{\mathrm{alloy}} = V_{\mathrm{Cr}}x_{\mathrm{Cr}} + V_{\mathrm{Co}}x_{\mathrm{Co}} + V_{\mathrm{Ni}}x_{\mathrm{Ni}}. \tag{4.1}$$

Following their approach, structural relaxations were performed for several ordering models applied to CrCoNi, $Cr_{10}Co_{13}Ni_{13}$, $Cr_{13}Co_{10}Ni_{13}$, $Cr_{13}Co_{13}Ni_{10}$. Resulting V_{alloy} values are plotted in the composition space of Fig. 4.5(a). In addition to the aforementioned simple structural and spin-ordered models, two variants of the spin-ordered state were also considered, containing either minimal or maximal ordering of Co atoms (see Ref. [3] for details).

Several planes representing distinct fits of Eq. (4.1) are drawn in Fig. 4.5(a), including one for quasirandom structures (blue, dashed edges), which were also computationally examined by Yin *et al.* [40]. For a given ordering model, compositionally disproportionate volume change can tilt the plane of Eq. (4.1) relative to the random state, yielding different partial molar volumes. While the simple structural model only modestly affects total volume relative to the quasirandom state, the formation of a $\mathrm{Cr}_{\downarrow}$ sublattice and corresponding growth of those moments (as in Fig. 4.3) leads to significant volumetric dilation, especially at higher Cr concentrations. The most extreme shift occurs under maximal spin-ordering, corresponding to the orange plane with a dotted border in Fig. 4.5.

Fig. 4.5(b) contains partial molar volumes determined from the different models of order considered in Fig. 4.5(a). Results for quasirandom configurations, or even those containing simple structural ($\alpha_{\mathrm{CrCr}} = 0.5$) SRO, are not far from the (quasirandom) computational predictions of Ref. [40]. Volume increases under further degrees of order, however, shift V_{Ni} and V_{Cr} toward the experimental results of Yin *et al.* [40], although some discrepancies remain, particularly for V_{Co} [40].

As demonstrated in the previous subsection, composition-dependent ordering should be considered; while this opens many possibilities, the analysis of magnetization offers some guidance. Specifically, the data from Fig. 4.4 suggest that the spin-ordered model could explain the equiatomic point well, while a sample with approximately $x_{\mathrm{Cr}} < 0.3$ is better represented by the simple structural model. If the configurations with reduced Co similarly contain less ordering of Co (min. spin-order), then a "hybrid" fit can be constructed, as graphed in Fig. 4.5(a) (green, dot-dashed border). More explicitly, the hybrid model assumes simple structural order at $Cr_{10}Co_{13}Ni_{13}$, spin-order for CrCoNi and $Cr_{13}Co_{13}Ni_{10}$, and "min. spin-order" at $Cr_{13}Co_{10}Ni_{13}$. Fitting to this combination of models predicts partial molar volumes, shown on the right of Fig. 4.5(b), that reproduce experiments within established levels of error for this type of calculation [40].

While it is important to note the possibility of significant magnetovolume coupling, it is admittedly difficult to imagine this exact scenario occurring physically. Nonetheless, these results raise the possibility that other magnetic phenomena, such as temperature-induced

longitudinal spin fluctuations, could tilt the volume-composition in a manner consistent with experiment, and that the anomalies of Ref. [40] do not disprove the accuracy of ground state DFT.

4.3 Discussion

It should be emphasized that the proposed ordering principles largely hold in hcp structures, as shown in Fig. 4.2. Thus, the positive stacking-fault energy determined in Ref. [65] arises simply from the disruption of fcc SRO by the imposition of hcp stacking. As seen in elemental Co and the calculations of Ref. [76], fcc CrCoNi is only stable at high temperatures, suggesting that the phase's low-temperature persistence could be supported by retained ordering. SRO of this nature could also explain why deforming CrCoNi induces thin layers of hcp stacking along twin boundaries [77], where local ordering has been broken, but not any larger regions of the theoretically more stable phase. In Ref. [78], we further speculated how the remarkable low-temperature work hardening of CrCoNi could in part originate from the ordering-limited formation of planar defects, which were observed at a scale that could possibly impede dislocation motion, but not one that would meaningfully reduce ductility. This behavior is contrasted by certain non-ordering Co-Ni alloys, which similarly retain a metastable fcc phase after quenching, but exhibit both spontaneous and deformation-induced martensitic phase transformations [79]. Both the nature of deformation in CrCoNi, and it apparent invariance to thermal treatment [18,19], could be interpreted to support the presence of comparably significant SRO in all experimentally tested samples.

In any case, the creation of simple and transferable ordering models can greatly facilitate the study of such scenarios, as demonstrated by the simulation of experiments concerning spontaneous magnetization and partial molar volumes. The ability of SRO to reproduce these otherwise unexplained measurements offers the possibility that the experimental samples contained order following, to various extents, the previously discussed principles. This hypothesis may seem striking given that none of the experimental samples were annealed in a manner intended to promote the development of order. However, SRO in CrCoNi has a large energetic driving force [64,65], requires a very short diffusion length, and is predicted to persist at high temperatures by multiple models [70,71]. In light of these factors, and the historical meausrements discussed in Ch. 2, an extremely rapid onset of SRO during the cooling of samples is not unimaginable.

Limited experimental evidence corroborates this picture [80]; for instance, the ferromagnetism predicted for random solid solutions has been observed in some thin films, which may be less prone to ordering at low deposition temperatures [81]. Severely deformed CrCoNi samples containing hcp martensite also exhibit some ferromagnetism [82], although the precise origin of the small reported moment is unclear. The magnetic properties of CrMnFeCoNi appear similarly sensitive to cold working and heat treatment [83], which could be at least partially explained by the effects of these processes on SRO. Some further investigation of this topic seems merited, although the study of alloys containing V in place of Cr may

prove more immediately enlightening given the previously mentioned questions regarding the magnetism of Cr [4].

Chapter 5

Theoretical antiferromagnetism of Cr-Ni

Copyright Notice

5.1 Introduction

Ni-rich Cr-Ni alloys have been studied for over a century on account of their extensive applications and intriguing process of chemical ordering. While elemental Cr forms body-centered cubic (bcc) crystals, about 36 at. % Cr is soluble in face-centered cubic (fcc) Ni. $CrNi_2$, the system's only experimentally observed intermetallic phase, emerges from these solid solutions as a $MoPt_2$-type lattice decoration—see Fig. 5.1(a)—below ∼863 K [84]. This relatively low ordering temperature kinetically limits the realization of $CrNi_2$, which forms nanoscale antiphase domains that slowly grow over thousands of hours of annealing [85]. Still, the structure has been observed in alloys with ∼25–36 at. % Cr [14, 84], with indications of a similar phase found in commercial Ni-based alloys [85, 86] and fcc medium/high-entropy alloys [23, 24] of current interest.

The gradual formation of $CrNi_2$ is associated with well studied "K-state" phenomena, including significant increases in hardness and resistivity, as well as lattice contraction [14, 85, 87]. Its magnetic properties, however, have largely escaped scrutiny. While elemental Ni is ferromagnetic (FM) below 631 K [88], the addition of Cr rapidly decreases both spontaneous magnetization and Curie temperature, resulting in a "quantum critical point" at about 11 at. % Cr [89, 90]. Alloys with greater concentrations of Cr are generally regarded as paramagnetic at all temperatures [91, 92], although evidence for a more nuanced picture will be discussed later.

Regardless of finite-temperature behavior, paramagnetism is not an electronic ground state and likely originates at least in part from thermally induced spin fluctuations, as

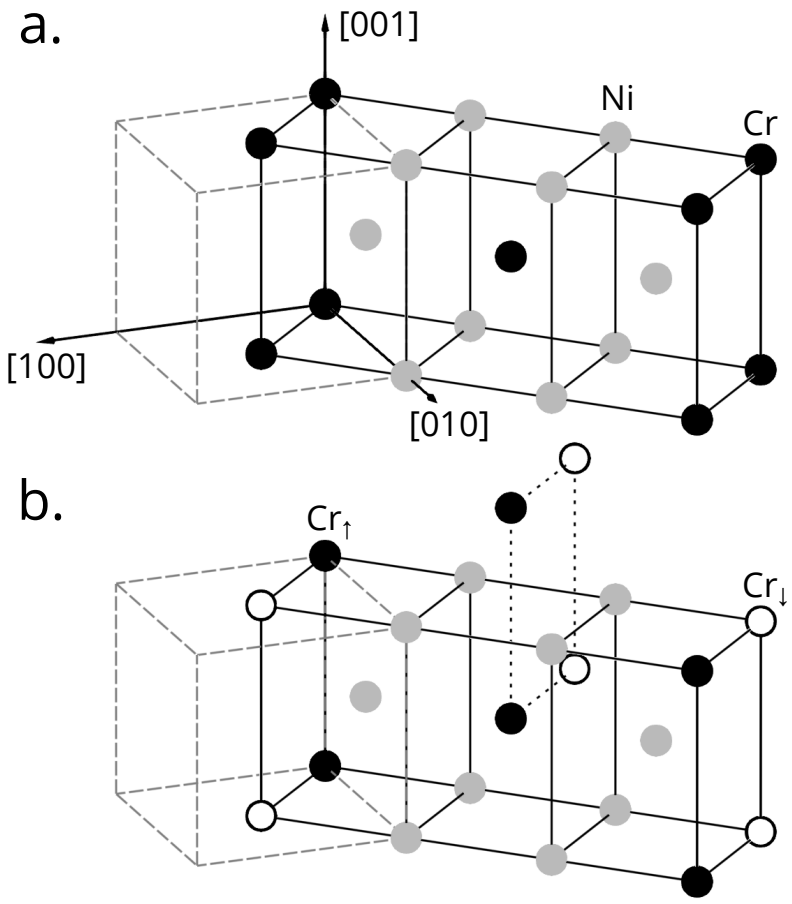

Figure 5.1: (a) The conventional unit cell of $CrNi_2$. Dashed lines and coordinate axes indicate the conventional fcc unit cell. (b) Proposed AFM ground state of $CrNi_2$, drawn on the same structure. Arbitrarily oriented "up" and "down" Cr moments are respectively represented using • and ∘ markers. The actual tiling supercell is larger and an extension of the central $(\bar{1}10)$ plane is included to fully depict the ordering.

have been theorized in chemically similar alloys [26, 93–95]. Many previous studies [28, 96–99], including high-throughput databases [100, 101], have predicted that $CrNi_2$ is nonmagnetic (NM) at 0 K; given the apparent lack of magnetic order (and desire to model high-temperature conditions), others have neglected spin-polarization entirely [102]. However, while standard techniques can easily simulate ferromagnetism, the convergence of antiferromagnetic (AFM) electronic structures requires the input of a specific magnetic symmetry, including a commensurate simulation supercell. (This is generally accomplished through qualitative initialization of local magnetic moments on atomic sites.) Both the primitive and conventional unit cells of $CrNi_2$ (see Fig. 5.1) consider all nearest-neighbor Cr pairs to be symmetrically equivalent, imposing identical magnetic states that preclude the realization of the simplest forms of antiferromagnetism. It is not clear whether any prior computational study of $CrNi_2$ investigated supercells compatible with AFM order, let alone seeded reasonable magnetic structures, motivating a revisitation of magnetism in Cr-Ni alloys under conventional electronic structure methods (see Sec. 5.2).

Section 5.3 details how previously overlooked AFM states theoretically exist for ordered Cr-Ni structures across a range of compositions. The antiferromagnetism of $CrNi_2$ is then further characterized in terms of a Heisenberg model with longitudinal spin fluctuations (LSFs). While the nature of magnetism at finite temperature remains unclear, the next section attempts to explain the ground state predictions in light of experimental findings, although it is concluded that further measurements are necessary.

5.2 Methods

For the first two parts of Sec. 5.3, collinearly spin-polarized density-functional theory (DFT) structure optimizations were performed using the Vienna *Ab initio* Simulation Package (VASP) [103]. (None of the considered structures contained geometric frustration that could be expected to elicit noncollinear moments and spin-orbit coupling is negligible at the energy scale of ordering.) Electronic states were represented in terms of plane-waves [104, 105] with a 520 eV cutoff and a linear k-point density of 0.15 Å. State occupancies were smeared to a width of 0.1 eV using a first-order Methfessel-Paxton method [106]. Atomic moments were conservatively integrated within 1 Å spheres so that all magnetization was contained within the Cr Bader surface [107]; more rigorous methods for determining local moments, such as the complete integration of Bader volumes, were complicated by the subsequent imposition of spin spirals. Cr sites were assigned initial moments of $\pm 2\,\mu_B$; Ni sites were also initialized with $1\,\mu_B$ moments, but expectedly demagnetized during the convergence of calculations unless specifically noted.

The treatment of electronic exchange and correlation (XC) requires some investigation. Section 5.3 considers both the local spin-density approximation (LSDA) and the generalized-gradient approximation (GGA), the former using Perdew and Zunger's [108] parametrization of Ceperley and Alder's [109] correlation energies and the latter according to Perdew, Burke, and Ernzerhof, either in the original formulation (PBE) [110] or as revised for solids (PBEsol)

[111]. Correlation energies were interpolated using the method of Vosko, Wilk, and Nusair [112]. For calculations at the experiment lattice parameter, PBE structures were scaled using values of 3.5240 Å for Ni, 2.8848 Å for Cr [113], and 3.562 Å for $CrNi_2$ [92].

On the basis of the results presented in Sec. 5.3, PBE was selected for all further calculations; this choice is largely motivated by results for elemental Cr, which require some further discussion. Namely, it must be noted that semilocal DFT fails to reproduce the experimental ground state of bcc Cr [114], which is a structurally incommensurate spin-density wave described by the wave vector $\boldsymbol{q} \sim 0.95\boldsymbol{b}_1$ [115], where $\boldsymbol{b}_1$ is the cubic reciprocal lattice vector. Still, the observed spin-density wave only slightly differs from the simple AFM structure predicted by DFT ($\boldsymbol{q} = \boldsymbol{b}_1$), corresponding to an energy difference of a few meV per atom in the present calculations. Absent further failures, DFT may still reasonably approximate the magnetic ground state of Cr, which provides an experimental benchmark for assessing predictions of antiferromagnetism in Cr-Ni alloys.

In order to better characterize the magnetism of $CrNi_2$, spin-wave calculations were performed in Sec. 5.3. In these simulations, noncollinear AFM structures were represented as plane waves of local magnetization density lying within the first Brillouin zone of a structurally minimal unit cell [116], as implemented in VASP. $CrNi_2$ was modeled using a static primitive lattice with $\boldsymbol{a}_1 = \frac{1}{2}[110]$, $\boldsymbol{a}_2 = \frac{1}{2}[\bar{1}21]$, and $\boldsymbol{a}_3 = [001]$ and, in reciprocal space, $\boldsymbol{b}_1 = \frac{1}{3}(420)$, $\boldsymbol{b}_2 = \frac{1}{3}(\bar{2}20)$, and $\boldsymbol{b}_3 = \frac{1}{3}(1\bar{1}3)$. (The exact structure was determined from the collinear ground state, restricting magnetovolume coupling and slightly exaggerating the magnetization energy; cf. Table 5.1.) Under this convention, the AFM configuration depicted in Fig. 5.1(b) corresponds to a $(\frac{1}{2}00)$ wave vector, with additional structures determined from modulations of this state; e.g., AFM decoration along [001] is represented by the wave vector $(\frac{1}{2}0\frac{1}{2})$. The longitudinal degree of Cr magnetization was allowed to relax in all calculations. Altogether, 111 wave vectors were chosen by interpolating among high-symmetry points near the region of AFM stability within the Brillouin zone.

5.3 Results

Magnetic ground state of $CrNi_2$

Metallic magnetism is typically understood in terms of two-site exchange couplings governed by Ruderman-Kittel-Kasuya-Yosida (RKKY) interactions, which decay according to the third power of distance in the long-range limit [117, 118]. Assuming AFM alignment of nearest-neighbor Cr spins, the $MoPt_2$-type structure of $CrNi_2$ can accommodate several distinct magnetic orderings depending on the nature of longer-range exchange interactions. As depicted in Fig. 5.1(a), Cr atoms occupy every third plane in the $(\bar{1}10)$ direction; these planes are offset such that, if nearest-neighboring Cr are AFM, every Cr-Cr bond between adjacent planes is balanced by an equidistant, opposite-spin counterpart (e.g., $\frac{1}{2}[\bar{1}21]$ and $\frac{1}{2}[\bar{2}11]$), preventing pairwise interactions between immediately neighboring planes from affecting the magnetic ground state. It is thus assumed that the type of exchange interaction

Table 5.1: Several possible magnetic configurations of $CrNi_2$ with AFM nearest $\left(\frac{1}{2}[110]\right)$ neighbors, according to several XC functionals. The first two columns indicate the type of magnetic ordering along the specified crystal direction. The third and fourth columns respectively give the average local moment magnitude and formation energy, while the last value is the change in energy relative to the NM structure. Calculations for AFM bcc Cr and NM $CrNi_2$ are provided for comparison.

[001]	$\frac{1}{2}[\bar{3}30]$	$\lvert m_{\mathrm{Cr}}\rvert$ (μ_B)	$E_{\mathrm{form.}}$ $\left(\frac{\mathrm{meV}}{\mathrm{atom}}\right)$	$E_{\mathrm{mag.}}$ $\left(\frac{\mathrm{meV}}{\mathrm{Cr}}\right)$
GGA-PBE/self-consistent lattice				
AFM	AFM	1.16	-26.7	-24.1
AFM	FM	1.20	-28.5	-29.4
FM	FM	1.29	-30.8	-36.4
FM	AFM	1.31	-31.9	-39.6
NM $CrNi_2$		—	-18.7	—
bcc Cr		0.98	0.0	-15.9
GGA-PBEsol/self-consistent lattice				
AFM	AFM	0.45	-41.7	-1.0
AFM	FM	0.56	-42.3	-2.7
FM	FM	0.74	-42.8	-4.4
FM	AFM	0.79	-43.0	-4.9
NM $CrNi_2$		—	-41.4	—
bcc Cr		0.34	0.0	-0.6
LSDA/experimental lattice parameter				
AFM	AFM	0.75	-40.0	-2.1
AFM	FM	0.83	-40.8	-4.7
FM	FM	0.92	-41.9	-7.9
FM	AFM	0.97	-42.4	-9.3
NM $CrNi_2$		—	-39.3	—
bcc Cr		0.64	0.0	-2.5
GGA-PBE/experimental lattice parameter				
AFM	AFM	1.30	-25.4	-41.8
AFM	FM	1.33	-27.4	-47.9
FM	FM	1.40	-30.0	-55.8
FM	AFM	1.41	-31.0	-58.7
NM $CrNi_2$		—	-11.4	—
bcc Cr		1.09	0.0	-28.3
GGA-PBEsol/experimental lattice parameter				
AFM	AFM	1.17	-31.3	-25.6
AFM	FM	1.21	-33.1	-30.8
FM	FM	1.28	-35.3	-37.4
FM	AFM	1.29	-36.1	-40.0
NM $CrNi_2$		—	-22.8	—
bcc Cr		0.97	0.0	-17.8

between second-nearest [001] neighbors fixes the ordering of a given $(\bar{1}10)$ plane. The relative order of the next-nearest $(\bar{1}10)$ planes then allows two possible magnetic structures for a given planar ordering, corresponding to either FM or AFM coupling between tenth-nearest $\frac{1}{2}[\bar{3}30]$ neighbors.

Altogether, these considerations allow four unique AFM structures, which are described in the first two columns of Table 5.1 in terms of [001] and $\frac{1}{2}[\bar{3}30]$ exchange couplings. The local moments and energies of these structures were calculated using several XC functionals and are tabulated in subsequent columns. Both formation energies (E_{form}), relative to AFM bcc Cr and FM fcc Ni, and magnetization energies (E_{mag}), relative to NM structures, are given; the latter are normalized per Cr atom as Ni sites are NM under all of the considered scenarios. Calculations for NM $CrNi_2$ and elemental Cr are also provided.

Under the LSDA, the equilibrium lattice of $CrNi_2$ is NM, but this is hardly surprising as the theory also fails to self-consistently reproduce the antiferromagnetism of bcc Cr, to say nothing of its inaccuracy for Ni. Imposing the experimental lattice parameter stabilizes magnetic order in both Cr and $CrNi_2$, although, at least in the former case, the magnetization energy is unphysically small [114]. The calculated formation energies, on the other hand, are somewhat larger than expected from the relatively low experimental order-disorder transition temperature [102,119]. In contrast, the PBE-based calculations predict a reasonable magnetization energy for Cr and even stronger magnetism in $CrNi_2$. (It should be noted that the PBE local moments of bcc Cr appear somewhat larger than experiment [114,120], although assigning AFM moments is somewhat less straightforward than determining FM magnetization.) Using PBEsol leads to unrealistically weak antiferromagnetism in Cr, although the magnetization energy of $CrNi_2$ remains several times larger and PBEsol calculations at the experimental lattice parameter resemble equilibrium PBE.

Regardless of the specific XC functional, the relative hierarchy of magnetic interactions is clear: [001] neighbors align ferromagnetically, as expected from RKKY theory, while interplanar $\frac{1}{2}[\bar{3}30]$ neighbors slightly favor AFM coupling, as depicted in Fig. 5.1(b). Moreover, in all physically plausible scenarios in which Cr is correctly AFM, the magnetization energy of $CrNi_2$ is more than twice that of bcc Cr on a per Cr basis; the local moments of $CrNi_2$ are also consistently larger. Quantitatively, PBE clearly provides the most reasonable description of Cr and is used for the remainder of the study. While PBE produces the largest absolute magnetization energies, the predicted ratio of $E_{\text{mag}}^{\text{CrNi}_2}$ to $E_{\text{mag}}^{\text{Cr}}$ is comparable to or significantly less than other calculation schemes. Its formation energies also seem reasonable [102,119], although these values are notably affected by magnetic order; the formation energy of the optimized magnetic structure ($-31.9\,\text{meV/atom}$) is 70% larger in magnitude than the NM equivalent ($-18.7\,\text{meV/atom}$). All PBE formation energies are plotted in Fig. 5.2.

Magnetism of other fcc orderings

While only $MoPt_2$-type ordering has been observed in fcc Cr-Ni, the possibility of additional phases has received some prior attention. Regardless of composition, the system's high-

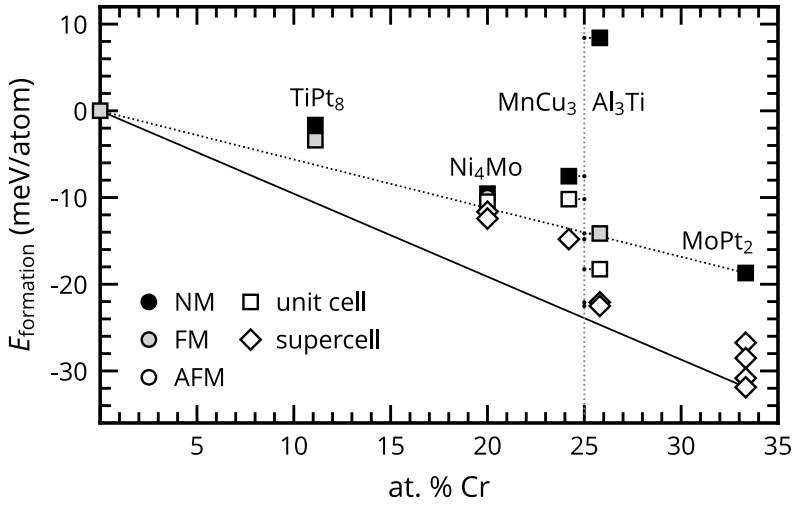

Figure 5.2: Calculated formation energies of various orderings discussed in the text as a function of composition. Annotations provide the prototype of each structure, with markers indicating the type of simulation cell and converged magnetic order. (A "unit cell" may be primitive or conventional.) The dotted and solid lines represent the convex hulls of stable structures based, respectively, on nonmagnetic and magnetic $CrNi_2$.

temperature chemical short-range order maximizes diffuse scattering intensity at the $(\frac{1}{2}10)$ special point in reciprocal space rather than the $(\frac{2}{3}\frac{2}{3}0)$ point expected for $MoPt_2$ [16, 17, 22, 121], as can be explained by nucleation considerations [21]. Maxima at $(\frac{1}{2}10)$ are instead associated with the NiMo (A_2B_2), Al_3Ti ($D0_{22}/A_3B$), and $MnCu_3$ ($D0_{60}$) [102] prototypes, which have been considered by a number of previous studies.

As for $CrNi_2$, the AFM ground states of other structures appear to have been overlooked with significant energetic consequences. For example, the NM calculations of Ref. [102] suggest that $MnCu_3$ and Ni_4Mo-type ($D1_a$) orderings could occur at low temperatures. The introduction of antiferromagnetism, however, not only further stabilizes $CrNi_2$, but also inverts the relative favorability of $MnCu_3$ and otherwise high-energy Al_3Ti, as shown in Fig. 5.2 (relative to AFM bcc Cr and FM fcc Ni). Figure 5.3 depicts the AFM ground states predicted for the (a) Al_3Ti and (b) $MnCu_3$ prototypes, which were identified through a process similar to that for $CrNi_2$. AFM decorations of the Ni_4Mo-type structure were also examined, although with minimal energetic effect.

Reference [28] additionally calculated that a $TiPt_8$-type [122] ordering of $CrNi_8$ was stable relative to NM $CrNi_2$ and FM Ni. At this composition, Ni atoms retain FM magnetization that induces opposite moments in distantly spaced Cr sites, leaving little opportunity for other forms of antiferromagnetism. As shown in Fig. 5.2, this structure was found to be slightly higher energy than in Ref. [28], although the disagreement is within the range

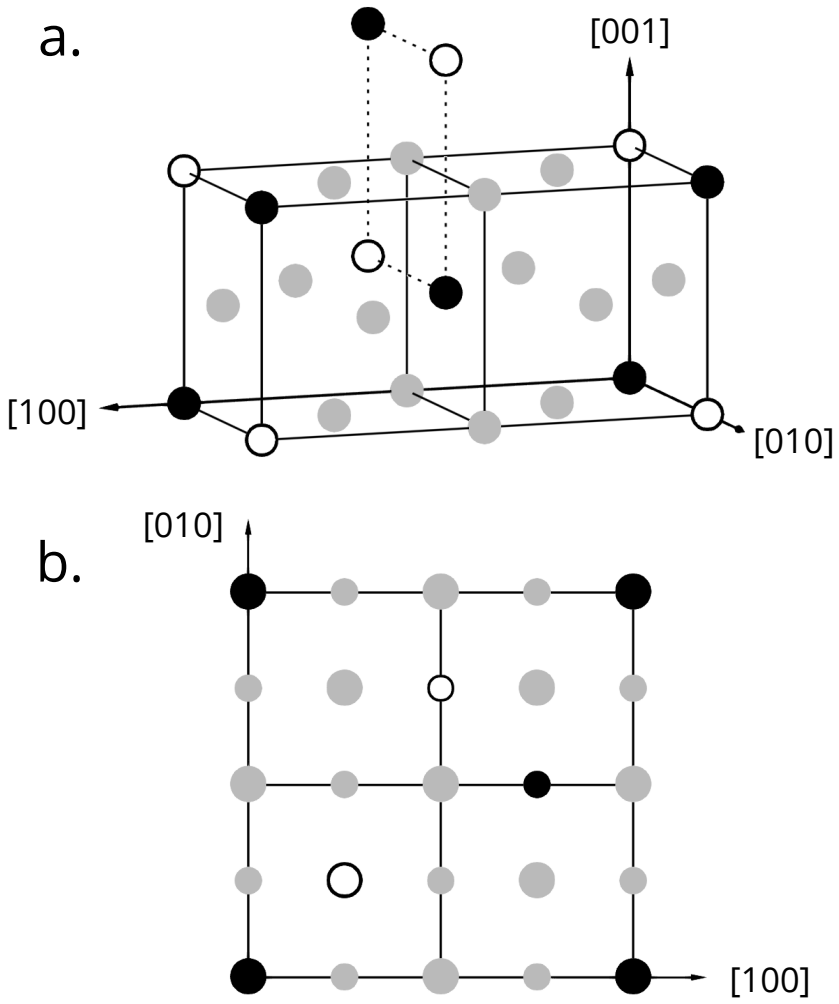

Figure 5.3: Proposed AFM ground states for the (a) Al_3Ti-type and (b) $MnCu_3$-type orderings of $CrNi_3$, illustrated in the manner of Fig. 5.1(b). The perspective of (b) is along [001], in which Cr moments are AFM. Atomic sites are drawn with different sizes to illustrate alternating (001) and (002) planes. While $MnCu_3$-type order is electronically more favorable, exchange interactions render Al_3Ti-type order lower energy, although neither is expected to be stable.

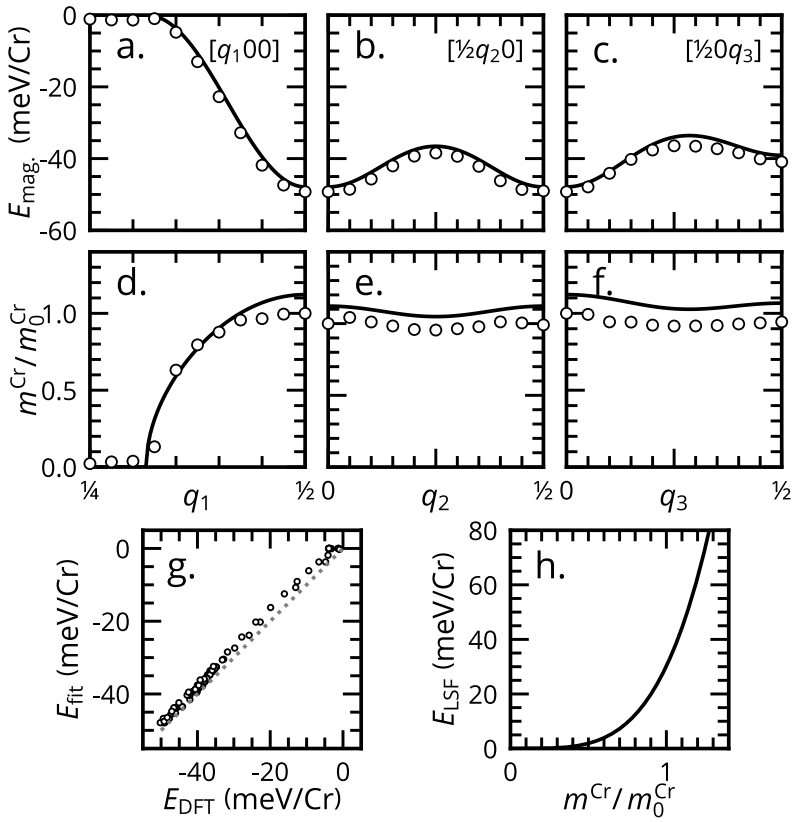

Figure 5.4: (a-c) *Open circles*: DFT energies of spin spirals representing modulations of the AFM ground state along the reciprocal lattice vectors of $CrNi_2$, as indicated with fractional coordinates—the structure in Fig. 5.1(b) corresponds to $(q_1 q_2 q_3) = \left(\frac{1}{2}00\right)$. *Solid lines*: equivalent values determined using Eq. (5.1) and Table 5.2. (d-f) As above, relaxed Cr moments from the same calculations and minimum energy values according to the effective Hamiltonian. (g) The energies of all considered spin spirals, as determined from the Hamiltonian vs. as calculated with DFT. (h) Energy contribution from the longitudinal term of Eq. (5.1) as a function of local moment.

expected from differences in simulation parameters.

Magnetic parametrization of $CrNi_2$

The introduction of AFM order further stabilizes $CrNi_2$, confirming the unique importance of this phase. Its theoretical magnetic structure can be more completely characterized in terms of a Heisenberg model of exchange interactions. The inconstant local moment recorded in Table 5.1, as well as instability of FM $CrNi_2$, indicates that the magnitude of Cr local moment

Table 5.2: Effective Cr-Cr exchange parameters of Eq. (5.1) fit to DFT calculations for spin-spirals in ordered $CrNi_2$. The longitudinal energy is fully accounted for by $J_2 = 31.95\,\text{meV}$. Neighbor directions ($\boldsymbol{R}_{ij}$) are expressed in terms of the fcc lattice parameter (a) for the structure depicted in Fig. 5.1. The square of each neighbor distance is provided to simplify notation.

$\boldsymbol{R}_{ij}$ (a)	R_{ij}^2 (a^2)	degeneracy	J_{ij} (meV)
$\frac{1}{2}[110]$	1/2	2	-18.6
$[001]$	1	2	0.71
$\frac{1}{2}[112]$	3/2	4	-0.36
$\frac{1}{2}[\bar{1}21]$	3/2	8	—
$[110]$	2	2	14.91
$\frac{1}{2}[\bar{3}01]$	5/2	8	—
$[111]$	3	4	—
$\frac{1}{2}[\bar{1}23]$	7/2	8	—
$[002]$	4	2	—
$\frac{1}{2}[\bar{3}30]$	9/2	4	-0.45
$\frac{1}{2}[033]$	9/2	8	—
$\frac{1}{2}[114]$	9/2	4	-0.57
$\frac{1}{2}[141]$	9/2	8	1.43
$[\bar{1}20]$	5	4	—
$\frac{1}{2}[332]$	11/2	4	—
$\frac{1}{2}[\bar{3}32]$	11/2	4	-0.99

is an important variable, as previously noted in austenitic stainless steels [26]. Changes in energy associated with such longitudinal spin fluctuations (LSFs) were accounted for by a phenomenological Landau-type expression, i.e. an energetic term proportional to the first few even powers of per site local moment [123–126]. Given the subjectivity inherent in localizing AFM moments, it is helpful to define a dimensionless effective spin $\boldsymbol{\mathcal{S}} = \boldsymbol{m}/m_0$, where $\boldsymbol{m}$ are classical magnetic moments (i.e., quantum expectation values) computed from density-functional theory (DFT) and m_0 refers to the ground state structure ($1.31\,\mu_\text{B}$ per Table 5.1). For Cr sites indexed by i and j, the model Hamiltonian takes the form

$$H = \sum_i \sum_{p=1}^{p_\text{max}} J_p \, \boldsymbol{\mathcal{S}}_i^{2p} - \sum_{i,j} J_{ij} \, \boldsymbol{\mathcal{S}}_i \cdot \boldsymbol{\mathcal{S}}_j \tag{5.1}$$

where J_p parametrize single-site LSFs and J_{ij} describe exchange between Cr atoms at sites i and j.

J_p and J_{ij} were fitted to reproduce the energies of magnetic structures represented by spin spirals, which can be efficiently computed using Bloch's theorem; see Sec. 5.2 for details. As an illustrative example, Fig. 5.4 shows the energies (a-c) and local moments (d-f) of

spirals representing modulations of the ground state along the reciprocal lattice vectors of the primitive unit cell.

Consideration of the sixteen nearest Cr-Cr interactions, which are described in the first three columns of Table 5.2, was required to reasonably represent all the magnetic configurations, although only eight distinct instances of J_{ij} were determined to be nonzero. The AFM $\frac{1}{2}$[110] interaction is expectedly the largest, although, interestingly, FM coupling between [110] neighbors in the same direction appears nearly as strong. All other exchange pairs are individually weaker by an order of magnitude, although they are more frequent (see the third column) and still significantly affect energies. The LSFs of Cr appear well described by a single $\boldsymbol{\mathcal{S}}^4$ term with $J_2 = 31.95\,\text{meV}$, which is plotted in Fig. 5.4(h). For spin-Hamiltonian calculations, the optimum local moment of a given spin wave was analytically determined from the fitted parameters. Both DFT energies and magnetic moments are replicated by the model, as shown in Fig. 5.4; since local moments are at no point explicitly fitted, faithful reproduction of these values suggests that the relevant physics are largely captured.

The exchange parameters calculated for $CrNi_2$ are at least qualitatively applicable to the other considered structures, the magnetization energies of which can be largely explained by the frequency of the two strongest Cr-Cr exchange pairs, $\frac{1}{2}$[110] and [110]. In the $MnCu_3$ structure depicted in Fig. 5.3(b), for instance, Cr have one $\frac{1}{2}$[110] and zero [110] Cr neighbors and consequently exhibit weak AFM coupling. In contrast, the (100) planar ordering of Cr in Al_3Ti provides four [110] Cr neighbors per Cr atom, effecting a several times larger magnetic ordering energy. Lacking Cr nearest neighbors, the Al_3Ti structure also accommodates a previously theorized [101] FM structure that abuts the convex hull of NM $CrNi_2$ in Fig. 5.2; this result illustrates how the partial consideration of spin polarization can be misleading even if, largely by happenstance, the qualitative picture of ground state phase stability in Cr-Ni remains unchanged.

Unfortunately, this simple model is likely not sophisticated enough to quantitatively predict the finite-temperature behavior of $CrNi_2$, even if the DFT results are largely physical. While the fitted parametrization accurately describes periodic deviations from the ground state, the effective exchange parameters of less ordered configurations can greatly differ [127] and Hamiltonians fitted exclusively to ordered configurations are known to poorly estimate Néel temperatures [93]. It is also less obvious how to model the majority element of Ni, which is NM in all ground state calculations, but may play a significant role at temperature due to LSFs, if to an unclear end. Perfectly disordered Ni moments should, on average, contribute zero net exchange to Cr sites, although it is easy to imagine random fluctuations locally destabilizing AFM order. Further, simulations of highly itinerant Cr moments should be validated in the pure element and I was unable to construct an equivalent model that could satisfactorily describe the antiferromagnetism of bcc Cr. (This is not entirely surprising, as the nominal disordering of bcc Cr hardly resembles a classical phase transition [128].)

5.4 Discussion

Even without finite-temperature calculations, the basic prediction of antiferromagnetism in $CrNi_2$ can be assessed in light of existing experimental data. If $CrNi_2$ is not in fact AFM at 0 K, the calculations of Sec. 5.3 would represent a fairly spectacular failure of a theory that otherwise reasonably describes the magnetism of 3*d* transition metals and would be an important finding in of itself. Such an error could originate from an overestimation of exchange interactions by the GGA, which has been previously postulated for Cr [114, 129]. Sill, even if the employed methods involved significant systematic error, all calculations found that the magnetic subsystem of $CrNi_2$ was significantly stronger than that of pure Cr. Given that bcc Cr has a nominal Néel temperature of 311 K [120], it seems plausible that magnetic order in $CrNi_2$ could persist well above ambient temperatures; naively scaling T_N^{Cr} according to the ratio of PBE magnetization energies would suggest $T_N^{CrNi_2} \sim 775$ K.

There has been some recent interest in the role of magnetic interactions—particularly those of Cr—in the chemical ordering of both steels [26, 98] and medium/high-entropy alloys [3, 11, 28, 69, 130], largely on the basis of DFT computations that have been called into question by some [40, 68]. (This is to say nothing of how disordered moments can affect properties such as stacking fault energies at finite temperatures [95, 131, 132].) $CrNi_2$ should provide a representative, experimentally accessible benchmark to test theoretical predictions concerning the role of magnetism in transition metal alloys that are not simple ferromagnets.

If $CrNi_2$ is indeed AFM at 0 K, the corresponding magnetic order-disorder transition should be detectable under calorimetry and magnetometry, although the Néel temperature is very much uncertain. Unfortunately, the experimental characterization of ordered $CrNi_2$ is incomplete; the fully formed intermetallic phase is of little practical interest given the deleterious effects of ordering on mechanical properties, to say nothing of its sluggish formation. Perhaps most relevantly, Ref. [92] measured the heat capacity of samples that were quenched after annealing at 773 K for up to 2900 hours. They reported specific heat values from 573 to 1073 K, observing a single peak at the ∼863 K chemical order-disorder transition that increased in magnitude with annealing; Refs. [23, 133, 134] provide similar results within this temperature range. The absence of lower-temperature calorimetry seemingly allows the possibility that a Néel transition below ∼550 K has simply escaped detection. While the oversight of a magnetic transition in such a well studied system would be surprising, it does not seem out of the question, particularly if antiferromagnetism is restricted to the fully ordered phase. Alternatively, it is interesting to consider the possibility of AFM order coupling to the well known chemical order-disorder transition at ∼863 K.

Limited experimental data actually support the possibility of AFM order in Cr-Ni alloys, which was in fact first theorized by Ref. [135] on the basis of neutron scattering in nominally disordered alloys with 5.98 at. % and 8.26 at. % Cr. At these compositions, the observed magnetism was interpreted as Cr moments collectively aligning antiparallel to otherwise FM Ni. These measurements are corroborated by the observation of heat capacity peaks in 6.72 and 8.94 at. % alloys at, respectively, 492 K and 675 K [136]. The temperature and magnitude of these features grows with Cr concentration, presumably merging with the aforementioned

structural transition occurring below 863 K in alloys with >20 at. % Cr [23], as is widely understood to represent chemical disordering. Indeed, Ref. [84] attributed the anomalies of Ref. [136] to a chemical SRO transition, although 492 K (219 °C) would be an extremely low temperature to detect chemical rearrangement given the experimental heating rate of 100 K/hour. Moreover, the specific heat curve of Ref. [136] appears to diverge in a manner that is far more consistent with long-range magnetic ordering than SRO. If Ref. [136] indeed detected antiferromagnetism at low Cr concentrations, it seems likely that some form of magnetic order persists up to the chemical order-disorder transition in $CrNi_2$.

Reference [137] appears to further corroborate this picture of magnetism, reporting susceptibility features consistent with an AFM transition in the range of 200–300 K for alloys with 8.75 at. % and 11.1 at. % Cr. After 8 hours of annealing at 900 K, the presumed development of chemical SRO raised the apparent magnetic transitions to about 500–600 K. Curiously, Ref. [91] failed to reproduce the observations of Ref. [137], but instead found anomalies in the magnetic susceptibility of alloys with 16.6, 22.0, and 25.0 at. % Cr in the vicinity of the chemical ordering temperature. Reference [91] in fact attributed these features to $CrNi_2$, although it is unclear whether the measurements indirectly reflect a chemical SRO transformation or possibly reveal an explicitly magnetic transition. In related commercial alloys, the formation of $CrNi_2$-based phases has also been noted to affect magnetic properties, although an exact mechanism has not been proposed [86, 138].

If antiferromagnetism persists to high temperatures, its neglect would be expected to cause errors in prior ordering theory. For instance, Refs. [17, 22] derived pair potentials from scattering experiments that notably underestimated the chemical ordering temperature of $CrNi_2$, suggesting neglected interactions and inviting speculation as to the missing physics. However, lattice models fitted to NM [102] or mostly NM [119] DFT calculations slightly *overestimate* the ordering temperature of $CrNi_2$ after correcting incomplete pair potentials with many-body interactions. Barring a fortuitous cancellation of errors, the relative accuracy of these calculations implies that magnetism plays a negligible role in the ordering of $CrNi_2$. Still, it is worth noting that while the model of Ref. [102] largely reproduces the chemical SRO of Ref. [16], which examined samples that were quenched after equilibration at 828 K, it appears to overestimate the equivalent *in situ* measurements at 993 K (25 at. % Cr) and 1073 K (33 at. % Cr) [22]. If, very speculatively, magnetic order affected the chemical SRO of quenched samples and Ref. [102] overestimated electronic interactions in a manner compensating the omission of magnetism, the apparent discrepancy could be explained.

5.5 Summary & Conclusion

A complete treatment of magnetic order greatly affects the ground state energetics of Cr-Ni alloys under standard DFT, greatly increasing the stability of $CrNi_2$, which remains the only predicted ordered phase. The role of magnetism at temperature is less clear, with three plausible scenarios. In the first, the prediction of antiferromagnetism is simply erroneous and the application of the theory to similar systems should be reexamined. Alternatively, $CrNi_2$

could form an AFM structure at 0 K that disorders below ∼550 K with minimal impact on chemical bonding, although it would still be interesting to assess whether AFM order existed at ambient conditions. Most intriguingly, the experimental literature appears to offer the possibility of a magnetic phase transition coupling to the chemical order-disorder transition at 863 K. Further thermodynamic and magnetic measurements seem needed to determine the nature and role of magnetism in ordered $CrNi_2$, with additional study likely required for less ordered alloys of great practical interest.

This line of investigation motivated the next and final chapter, in which a method is developed for realistically and conveniently simulating the Heisenberg model at temperature. In practice, however, the approach proved incompatible with the continuous, phenomenological treatment of spin-fluctuations that was used to model the magnetism of Cr-Ni alloys.

Chapter 6

Realistic magnetic thermodynamics

6.1 Introduction

The Heisenberg model has been widely studied as both a classical and quantum description of crystal magnetism. In either interpretation, the Hamiltonian can be expressed as

$$H = -\sum_{i,j} J_{ij}\, \mathbf{S}_i \cdot \mathbf{S}_j \tag{6.1}$$

where i and j sum over lattices sites and J_{ij} is an interaction energy determined by the relative positions of i and j. Classically, $\mathbf{S}_i$ is a dimensionless spin vector proportional to local magnetic moment. While atomic magnetism has fundamentally quantum origins, the classical model largely accounts for the energies of *static* spin configurations, reproducing experimental magnon spectra and capturing magnetic contributions to the energies of electronic structure calculations [118, 139]. It does not, however, accurately describe thermodynamic properties below the magnetic disordering temperature [140,141] and, while alternatives have been proposed [140–147], the efficient simulation of finite temperature magnetism remains an outstanding problem in computational materials science.

The limited success of the classical Heisenberg model can be understood by regarding classical moments as the quantum expectation values of spin operators, as is detailed in the following section. With this perspective, the following section discusses Monte Carlo (MC) simulation of the Heisenberg model, a popular approach to calculating thermodynamic properties by probabilistically sampling the spin-configuration space. The deficiency of classical MC (CMC) methods is addressed and a more accurate, but similarly general, semiclassical MC (SMC) sampling technique is proposed, demonstrated, and discussed.

6.2 Results

Background and motivation

In the more physical quantum Heisenberg model, $\mathbf{S}_i$ operates on spinor $|\chi_i\rangle$ to measure the spin of lattice site i. N spins of quantum number s form a $(2s+1)^N$-dimensional Hilbert space. A canonical system in thermal equilibrium is described by density operator $\rho = \mathrm{e}^{-\beta H}/Z$, where partition function $Z = \mathrm{tr}(\mathrm{e}^{-\beta H})$ and β is the reciprocal product of Boltzmann's constant and temperature. Thermodynamic quantities corresponding to ensemble averages, such as energy or magnetization, are determined from ρ as $\overline{O} = \langle O \rangle = \mathrm{tr}(\rho\, O)$, where $\overline{O}$ denotes the ensemble average and $\langle O \rangle$ indicates a quantum expectation value.

Density operators are typically expanded as sums over energy eigenstate projectors, although the eigensystem of Eq. (6.1) is not generally solvable. Instead, states may be sampled through quantum MC (QMC) techniques [148], although current methods appear numerically unstable for Hamiltonians containing competing interactions [149], such as geometric frustration [150] or even values of J_{ij} with opposing signs [151], as is often the case in real materials. Compared to CMC, QMC is also far more conceptually and computationally complex, with simulation time scaling nonlinearly with system size [152].

Fortunately, magnets that are not significantly entangled may not require a full quantum treatment. Above some temperature, all equilibrium systems become unentangled, or separable [153], meaning that ρ may be expressed as a sum over product states $|\psi_p\rangle = |\chi_1\rangle \otimes |\chi_2\rangle \cdots \otimes |\chi_N\rangle$. Entanglement phenomena have been primarily identified in one or two-dimensional systems at low temperatures [154, 155], so it is assumed that separability is at least a very a good approximation for conventional three-dimensional magnets above a few degrees Kelvin.

Product states are attractive because their expectation values distribute across components of the tensor product [156], enabling effectively classical evaluation of the Heisenberg Hamiltonian. For product state $|\psi_p\rangle$, energy E_p can be determined as

$$\langle H \rangle_p = -\sum_{i,j} J_{ij}\ \langle \mathbf{S}_i \cdot \mathbf{S}_j \rangle_p = -\sum_{i,j} J_{ij}\ \langle \mathbf{S}_i \rangle_p \cdot \langle \mathbf{S}_j \rangle_p \,, \tag{6.2}$$

where $\langle O \rangle_p$ denotes $\langle \psi_p | O | \psi_p \rangle$. Equation (6.2) explains the success of the classical Heisenberg model in evaluating the energies of given magnetic structures, if classical $\mathbf{S}_i$ is understood as quantum $\langle \mathbf{S}_i \rangle_p$.

When $\langle \mathbf{S}_i \rangle_p$ is not prescribed, however—as is typically the case for thermodynamic ensembles—classical methods are far less accurate as determining *which* values of $\langle \mathbf{S}_i \rangle_p$ to consider requires significant approximation. Most notably, conventional CMC simulations sample spin states continuously, which is only justified in the limit of an infinite spin quantum number [157, 158]. Taking this limit provides the standard derivation of the classical Heisenberg model and leads to a scaling relation between the quantum (J_{ij}) and classical (J_{ij}^{∞}) interaction energies for spin quantum number s:

$$s(s+1) J_{ij} = s^2 J_{ij}^{\infty}. \tag{6.3}$$

Perhaps unsurprisingly, the assumption of infinite s causes unphysical thermodynamic behavior in not only CMC, but also classical spin dynamics simulations [159].

However, if $\langle \mathbf{S}_i \rangle_p$ were known for all the components of a separable representation, its thermodynamic properties could be calculated with quantum accuracy and classical convenience. For a separable ensemble that can be represented in terms of product states p, the average of observable O may be expressed as a classical sum, i.e.

$$\overline{O} = \frac{1}{Z} \sum_p \mathrm{e}^{-\beta E_p} \langle O \rangle_p \,, \tag{6.4}$$

as detailed in Supplementary Note 1 of Ref. [5]. For the determination of $\overline{E}$, Eq. (6.2) can be substituted into Eq. (6.4) such that the ensemble average is expressed in terms of $\langle \mathbf{S}_i \rangle_p$, with a similar procedure possible for other thermodynamic properties. Of course, identifying specific $|\psi_p\rangle$ or $\langle \mathbf{S}_i \rangle_p$ is no easier than determining eigenstates, but it may be feasible to approximate the *density* of product states more accurately than classical methods. Indeed, representatively sampling states in a high-dimensional configuration space is the fundamental purpose of MC simulations.

Previous efforts to improve the accuracy of classical simulations can be understood from this perspective. For example, spin-wave excitations can be quantized using Planck statistics, which reasonably describe magnetization behavior [139], although local updating methods are generally far more efficient for atomistic simulations. Ref. [145] approximates a density of states explicitly calculated using first-principles methods by introducing and adjusting an effective simulation temperature. This approach, which can be applied in continuous time spin dynamics as well as MC simulations [146], works well at low temperatures, but requires parameterization and underestimates [145] (or overestimates [146]) magnetization at intermediate temperatures. Somewhat similarly, Ref. [144] describes a method for empirically determining effective temperatures, while Ref. [147] reproduces a Planck distribution through careful control of a spin dynamics thermostat. It is also worth noting that the methods of Refs. [140, 144–146] directly depend on the Curie temperature (T_C), above which CMC is performed.

Semiclassical sampling by local quantization

Alternatively, the separable density of states may be more directly estimated according to a locally quantum approximation of state evolution. In the simplest form of CMC, a new state is trialed by mutating the (expected) spin of randomly selected site k, while the spins of all other sites $i \neq k$ are fixed. Trial $\langle \mathbf{S}_k \rangle$ is traditionally chosen with uniform probability for all directions, as is classically allowed. However, it is possible to introduce an approximate quantization by treating this ultimately fictitious permutation as a quantum problem.

In this approach, Eq. (6.1) can be reframed as a single-spin quantum Hamiltonian for site k,

$$H_k = E_{i \neq k} - \mathbf{S}_k \cdot 2 \sum_j J_{kj} \, \langle \mathbf{S}_j \rangle \,, \tag{6.5}$$

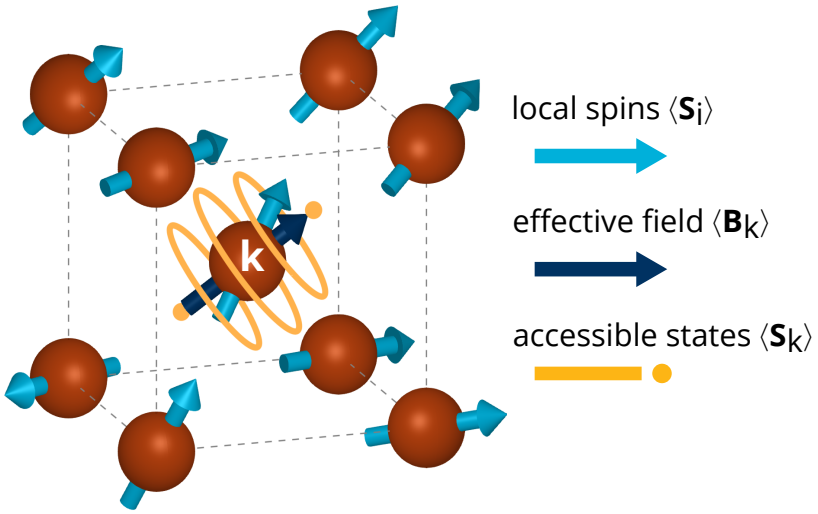

Figure 6.1: MC trial states allowed by local quantization. An illustration of the semiclassical spin sampling procedure on a bcc lattice with $s = 2$. Site k is randomly selected and the effective local field $\mathbf{B}_k$ is determined from the fixed spins of neighboring sites $\langle \mathbf{S}_j \rangle$ and the interaction energies J_{kj}. A new trial value of $\langle \mathbf{S}_k \rangle$ is randomly selected from the illustrated quantizations along $\mathbf{B}_k$.

where $\langle \mathbf{S}_j \rangle$ is the fixed spin of neighboring site j. (The factor of two originates from the double summation in Eq. (6.1)). As $E_{i \neq k}$ is constant, Eq. (6.5) has the elementary solutions of a spin in the magnetic field $\mathbf{B}_k = 2 \sum_j J_{kj} \langle \mathbf{S}_j \rangle$. Specifically, $\mathbf{S}_k$ is quantized along $\mathbf{B}_k$ with quantum number $m_s = -s, -s+1, \ldots, s$; its orthogonal components are inherently uncertain, but their expectation values precess around $\mathbf{B}_k$ in time.

The solutions of Eq. (6.5) can be statistically sampled according to the following semiclassical MC (SMC) procedure, which is illustrated in Fig. 6.1. For each MC step, site k is randomly selected and $\mathbf{B}_k$ is computed. A trial quantization along $\mathbf{B}_k$ (corresponding to some m_s) is chosen at random, defining the component of $\langle \mathbf{S}_k \rangle$ along $\mathbf{B}_k$; any remaining perpendicular component is then randomly chosen to account for continuous precession. The accessible trial states $\langle \mathbf{S}_k \rangle$ for a hypothetical scenario are drawn as rings around $\mathbf{B}_k$ in Fig. 6.1. The trial energy is computed and acceptance or rejection is determined according to the standard Metropolis criteria, after which a new k is chosen for the next step. In practice, SMC requires only marginally more effort than CMC, with spin quantum number s being the only additional parameter.

While the impact of multiple-spin interactions on quantization has been neglected, these solutions should still estimate the true distribution of product states better than purely classical methods, although the extent of the improvement is not immediately clear as separable solutions of large ensembles are generally intractable. In practice, the results are notably more accurate—indeed, the remainder of this paper demonstrates how locally quan-

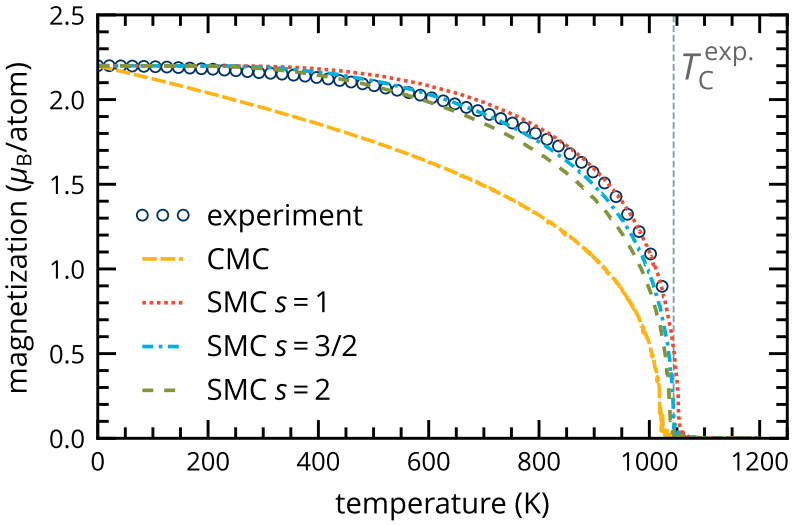

Figure 6.2: Spontaneous magnetization of iron. Spontaneous magnetization of elemental (bcc) Fe as a function of temperature, determined using CMC and SMC sampling for several spin quantum numbers s and experiment [88].

tized SMC reasonably describes thermodynamic properties across a wide temperature range, albeit with several caveats.

Magnetization of Fe

The zero-field spontaneous magnetization of body-centered cubic (bcc) Fe provides a classic benchmark for finite temperature magnetic predictions. Figure 6.2 shows measurements from Ref. [88] alongside notably differing CMC calculations (see Sec. 6.4 for details). The experimental ground state moment of $2.2\,\mu_B$/atom implies a quantum number of $s = 1.1$, neglecting orbital contributions that are suppressed under the system's cubic symmetry. As a transition metal, the itinerant magnetism of Fe is less than perfectly described by a collection of atomic spinors, but the standard Heisenberg model appears to provide a passable approximation [93]. Previous studies have modeled Fe by interpolating results for $s = 1$ and $s = 3/2$ [140], but for the purpose of demonstration, Fig. 6.2 shows distinct SMC magnetization curves for $s = 1$, $3/2$, and 2.

All the quantized calculations greatly improve upon CMC, although no single value of s exactly replicates experiment. Using $s = 1$, as is closest to the experimentally implied value, provides the best results near T_C, but not at lower temperatures, where $s = 3/2$ appears slightly more accurate. The next highest value of $s = 2$ is generally further from experiment, expectedly approaching the classical limit of infinite s—the gradual convergence of CMC

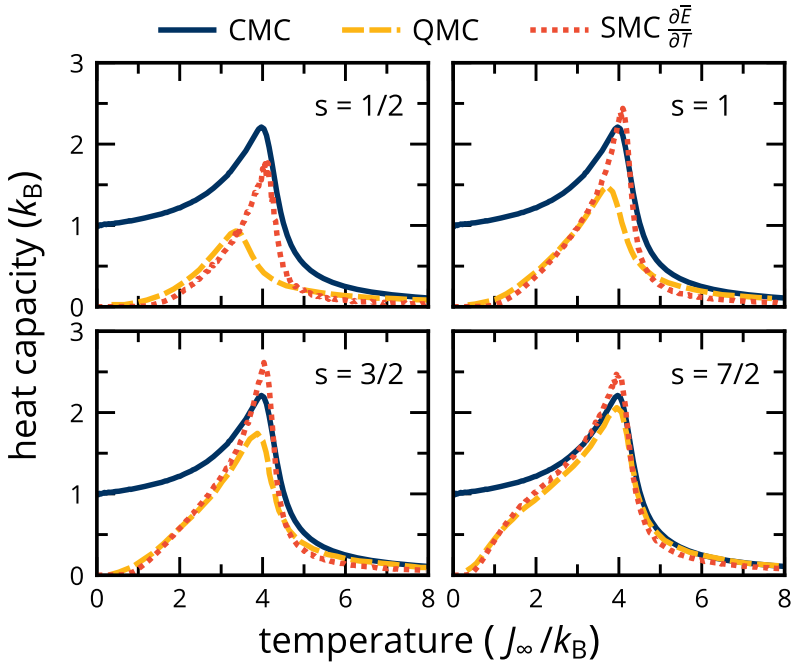

Figure 6.3: Heat capacity of a model ferromagnet for several spin quantum numbers. Heat capacity of a bcc nearest-neighbor ferromagnets for varying spin quantum number s, calculated via CMC, QMC (adapted from Ref. [140]), and SMC according to Eq. (6.6) Nearest-neighbor interaction energies are determined from classical J_∞ by Eq. (6.3).

and SMC is further shown in Supplementary Fig. 2 of Ref. [5]. Critical magnetization behavior is also examined in Supplementary Fig. 3 of Ref. [5]. Some remaining inaccuracies are discussed later, but the overall dramatic improvement clearly shows the potential of semiclassical local quantization.

Heat capacity and magnetic short-range order

While demonstrative, direct comparison of computational predictions to experiments is complicated by the many levels of approximation inherent in the theory. Fortunately, Ref. [140] provides effectively exact QMC heat capacities for a small bcc ferromagnet with nearest-neighbor Heisenberg interactions, which are shown in Fig. 6.3 for four spin quantum numbers in addition to infinite spin CMC (see Sec. 6.4 for details). Heat capacity is defined as

$$C = \frac{\partial \overline{E}}{\partial T}, \tag{6.6}$$

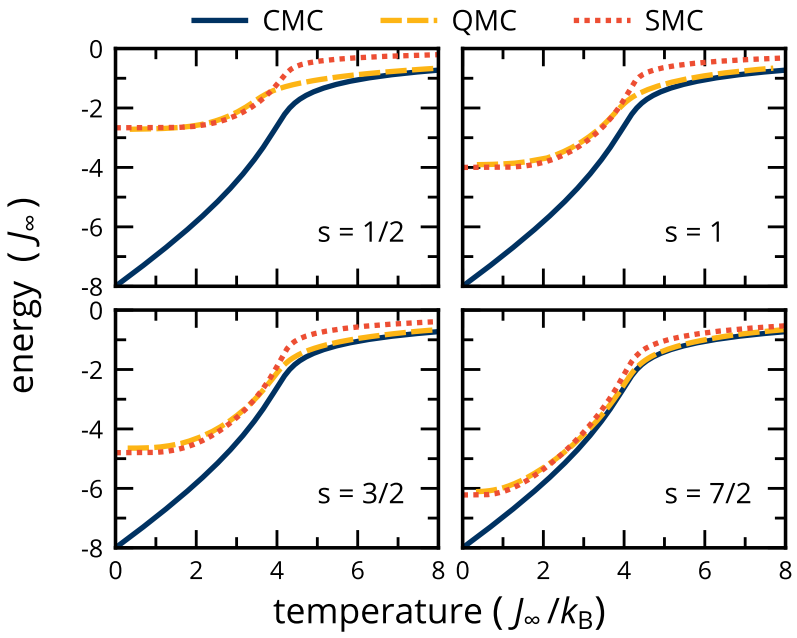

Figure 6.4: Energy of a model ferromagnet for several spin quantum numbers. Analogous to Fig. 6.3, the energies of a bcc ferromagnet with varying quantum number s according to CMC, QMC, and SMC. While SMC appears to reproduce the QMC of Ref. [140] below the disordering point, higher temperature energies are overestimated due to missing short-range order.

from which many other thermodynamic properties can be derived. Figure 6.3 shows that direct calculation of SMC heat capacity according to Eq. (6.6) largely reproduces QMC at lower temperatures, but results in significant errors around T_C, with altogether less improvement over CMC than seen in Fig. 6.2.

An explanation for excessive heat capacity in the critical region follows from Eq. (6.6); overestimation of heat capacity implies that simulation energies increase too rapidly with respect to temperature, which is explicitly shown in Fig. 6.4. Below T_C, semiclassical energies closely track QMC values, but magnetic disordering imparts a rapid increase in energy, resulting in an overestimation of energy that only gradually disappears at higher temperatures. Excess energies indicate that these simulations are less ordered than their QMC counterparts—since the error only becomes significant as long-range order disappears, it is apparent that locally quantized SMC systematically underestimates magnetic short-range order (MSRO).

In contrast, Fig. 6.4 shows how CMC energies are correct in the high-temperature limit despite significant error below T_C. Nonetheless, CMC and SMC predict very similar degrees

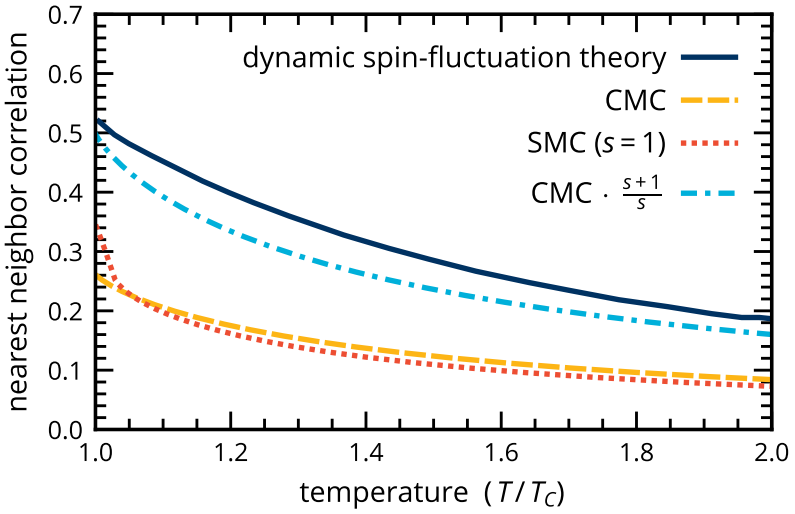

Figure 6.5: Magnetic short-range order in iron. Predictions of MSRO in bcc Fe by several theories, represented by the normalized nearest-neighbor spin-spin correlation: $\overline{\mathbf{S}_i \cdot \mathbf{S}_j} / \left(\overline{S}_i \overline{S}_j\right)$ for nearest neighbors i and j. Very similar CMC and SMC results are compared to dynamic spin-fluctuation theory [160], which predicts significantly larger MSRO due to quantization effects. The discrepancy can be mostly eliminated using the $\frac{s+1}{s}$ correction factor deduced from comparison of QMC and CMC.

of order above T_C, as demonstrated in Fig. 6.5 for nearest-neighbor spins in bcc Fe. These two observations imply that accurate CMC energies (and related properties, such as heat capacity) above T_C originate from the $\frac{s+1}{s}$ energetic scaling that was introduced in Eq. (6.3). Indeed, CMC has long been believed to underestimate MSRO on the basis of both experiment [161, 162] and theory [160, 163–165]. As a reference, Fig. 6.5 includes the significantly more ordered predictions [160] of dynamic spin-fluctuation theory [166], an advanced linear-response technique that does not explicitly consider local moments.

The observation that scaling CMC interaction parameters, as is required to preserve the Curie temperature, leads to accurate energies above T_C implies that a similar correction factor could recover realistic MSRO. This simple idea is tested in Fig. 6.5, which includes a version of the CMC spin-spin correlations multiplied *post hoc* by $\frac{s+1}{s}$ (for $s = 1.1$) that favorably compares to the theory of Ref. [160]. The remaining discrepancy may be attributable to the neglect of longitudinal spin fluctuations, which, although relatively small in Fe, can significantly affect MSRO [93], as well as the specific parameterization of the Hamiltonian.

The proposed scaling factor offers a path for correcting SMC, either *post hoc* or possibly through scaling interaction parameters J_{ij} as in CMC. With an optimized interpolation scheme smoothly introducing the scaling factor across the critical region, SMC could conceivably replicate QMC across across all temperatures in a manner reminiscent of previously

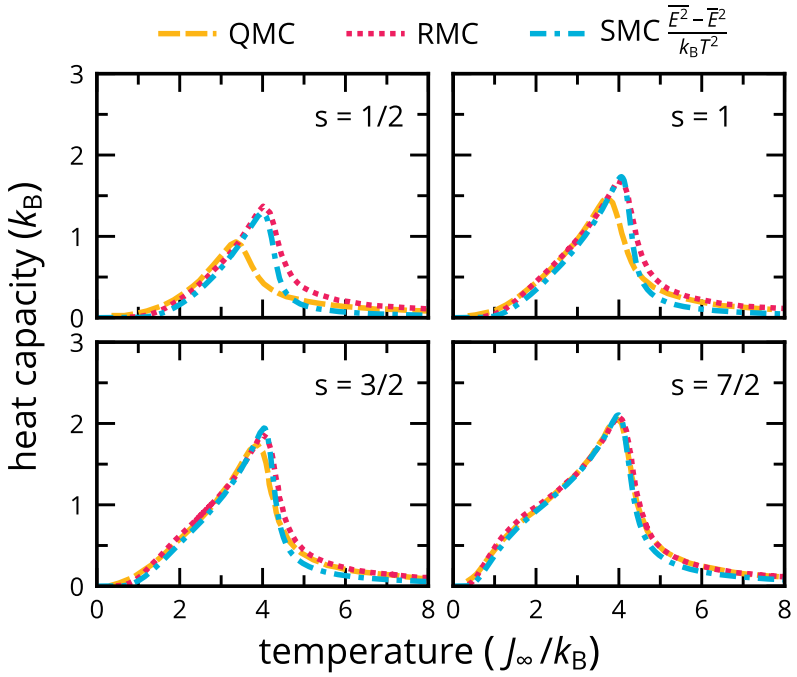

Figure 6.6: Improved and benchmarked heat capacities of the model ferromagnet. The QMC heat capacities from Fig. 6.3 (and ultimately Ref. [140]) compared to SMC calculations using Eq. (6.7), which are significantly more accurate than those shown in Fig. 6.3. The "rescaled" MC (RMC) results from Ref. [140], which provide a similar degree of accuracy, are also shown.

employed techniques [140,144]. However, this approach would compromise much of the convenience of SMC and a somewhat more straightforward method for recovering accurate heat capacities is explored in the following section.

Improved accuracy from fluctuations

Heat capacity may alternatively (and more conventionally) be calculated according to the fluctuation-dissipation theorem, i.e.

$$C = \frac{\overline{E^2} - \overline{E}^2}{k_B T^2}, \tag{6.7}$$

which must equal Eq. (6.6) for a statistically valid ensemble. However, SMC heat capacities determined in this manner, plotted in Fig. 6.6, notably differ from those previously calcu-

lated in Fig. 6.3—in fact, the values obtained from the fluctuation-dissipation theorem are significantly closer to the QMC of Ref. [140].

The disagreement between the heat capacities calculated from Eq. (6.6) and Eq. (6.7) can be attributed to a violation of balance by the SMC sampling procedure. Local quantization clearly does not satisfy *detailed* balance, as the local field at any site is frequently changed as neighboring spins are reoriented. If a spin is re-quantized along an updated local field, it is likely impossible to directly return to the prior state along the former quantization axis, which is a fundamental requirement for detailed balance. It is less immediately obvious that this procedure violates the statistically necessary condition of *balance* [167], but the difference between the two methods of calculating heat capacity, which are formally equivalent for a properly sampled ensemble, suggest an absence of balance. In contrast, if all spins are quantized along a fixed axis, then (detailed) balance is recovered and both methods of calculating heat capacity predict consistent values, which are similar to those of Fig. 6.3 (this is explicitly shown in Supplementary Fig. 1 of Ref. [5]). For local quantization, issues of balance could be circumvented by performing non-Markovian MC such as Wang-Landau sampling [168], which determines $\overline{E^2}$ from a sampled distribution of E such that Eq. (6.7) reproduces Eq. (6.6).

However, the degree of accuracy shown in Fig. 6.6 suggests that the fluctuation-based calculations are capturing more realistic physics. Despite excessive average energies due to the underestimation of MSRO, the SMC calculations appear to sample realistic energetic fluctuations. As shown in Fig. 6.3, the heat capacities of Eq. (6.6) are about as accurate as the best existing methods for (non-quantum) magnetic thermodynamics, exemplified by the "rescaled" MC (RMC) of Ref. [140], which applies an empirical correction factor to CMC based on lattice-specific QMC for a model Hamiltonian. The fluctuation-based approach thus seems very promising for practical calculations, although it would benefit from a more rigorous explanation for the demonstrated accuracy.

Antiferromagnetic susceptibility of $RbMnF_3$

While only ferromagnets have been considered up to this point, SMC sampling works similarly well for antiferromagnets, of which $RbMnF_3$ is one of the simplest examples. In this compound, Mn ions form a simple cubic sublattice with $s = 5/2$ and effectively nearest-neighbor exchange interactions [170]. Figure 6.2 shows the zero-field parallel susceptibility ($\chi^{\parallel}$) of $RbMnF_3$, both from experiment [169] and calculated with CMC and SMC via the fluctuation-dissipation theorem:

$$\chi^{\parallel} = \frac{\overline{\mathbf{M}^2} - \overline{\mathbf{M}}^2}{k_B T}. \tag{6.8}$$

Both axes have been scaled relative to T_N values to ease comparison with experiment. SMC is expectedly far more accurate than CMC below the disordering point, although $\chi^{\parallel}$ is somewhat underestimated at very low temperatures. Classical $\chi^{\parallel}$ appears slightly closer to

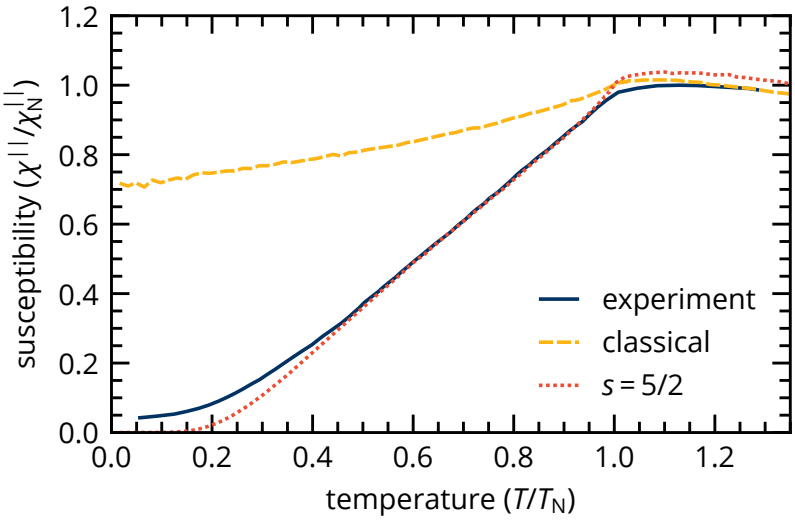

Figure 6.7: Antiferromagnetic susceptibility of $RbMnF_3$. Parallel magnetic susceptibility of the Heisenberg antiferromagnet $RbMnF_3$ as a function of temperature, calculated using CMC and SMC ($s = 5/2$). Experimental data is from Ref. [169]; all values are normalized relative to the Néel point to ease comparison.

experiment above T_N, likely reflecting the underestimation of MSRO by local quantization, although the choice of scaling could also affect the alignment of these values.

6.3 Discussion

The use of fluctuations for thermodynamic calculations largely resolves the primary source of error in SMC, but a few issues remain. In particular, local quantization systematically undersamples low-temperature excitations, which can be seen across a range of properties in Figs. 6.2, 6.6, and 6.7. Magnetization, for instance, should scale as an exponential of temperature in the 0 K limit, but it appears asymptotic in Fig. 6.2—as shown more clearly in Supplementary Fig. 4 of Ref. [5], SMC magnetization does not significantly deviate from the ferromagnetic state below $\sim T_C/5$. In reality, excitations in this region are dominated by long-wavelength spin-waves, which, while theoretically compatible with SMC, do not appear adequately sampled by local quantization. The omission of these excitations similarly explains a slight underestimation of heat capacity and susceptibility at low temperatures, as these properties reflect, respectively, energetic and magnetic fluctuations.

The absence of non-local quantizations may also be seen at higher temperatures. As shown in Fig. 6.6, QMC predicts slightly lower critical temperatures for $s = 1/2$ and $s = 1$ than for higher spin simulations, an effect which is not captured by SMC. For these lower

quantum numbers, the locally allowed quantizations are limited and higher in energy, leaving room for lower energy, longer range excitations to play a role in the disordering transition, slightly reducing T_C from the classical values. Single-site quantization also appears to inadequately predict MSRO, as seen in Fig. 6.4, with the implication that quantum MSRO originates from quantization states involving multiple spins.

Hopefully this work will motivate further study and development of semiclassical sampling methods, including resolutions of these issues. One apparent next step would be the simultaneous quantization of multiple neighboring spins, analogous to cluster flipping algorithms employed in CMC simulations [171]. When permuting multiple spins, new states could be drawn from the separable component of the local exact solution, which could be easily precomputed for small clusters. While extracting product states from these solutions may be nontrivial, their inclusion could allow lower energy excitations that improve simulation accuracy at low temperatures and promote high-temperature MSRO.

Opportunities for improvement notwithstanding, the simplest form of locally quantized SMC appears to provide a physics-based, parameter-free method for calculating magnetic contributions to thermodynamic properties that is at least as accurate as current methods with increased convenience and generality.

6.4 Methods

Simulations of Fe (Figs. 6.2 and 6.5) used ten values of J_{ij} from Ref. [118] for atomic separations up to and including $\mathbf{r}_{ij} = \left[\frac{3}{2}\frac{3}{2}\frac{3}{2}\right]$, which is associated with an energy several times larger than that of any longer range interaction. The selected J_{ij} predict a T_C close to the experimental value, although, given the limitations of the Heisenberg model [93], inaccuracy of the local-density approximation used in parameterization [172], and neglect of temperature scaling and phonon coupling [173, 174]—among other factors—the degree of accuracy presumably involves some cancellation of errors. After an equivalent period of equilibration, 10^5 MC passes were performed for $2.5 \cdot 10^5$ atoms over 1250 temperatures. For Fig. 6.5, similar simulations were performed at intervals of 5 K.

Simulations for Figs. 6.3, 6.4, and 6.6 considered 512 spins to match the QMC of Ref. [140]; $5 \cdot 10^6$ MC passes were performed at 256 temperatures. Calculations of susceptibility in $RbMnF_3$ for Fig. 6.7 involved 10^6 passes for $1.25 \cdot 10^5$ magnetic sites.

In the case of $\mathbf{B}_k = \mathbf{0}$, the local Hamiltonian of Eq. (6.5) imposes no specific quantization, so trial $\mathbf{S}_k$ should be oriented randomly. While irrelevant for most simulations, this procedure ensures that $s = \frac{1}{2}$ SMC trajectories with initially collinear spins are not restricted to the original quantization axis (i.e. an Ising model), as would otherwise occur. In practice, these calculations were initialized with randomly oriented spins to avoid any such issues.

References

[1] F. Walsh, A. Abu-Odeh, and M. Asta, MRS Bull. (to be published).

[2] F. Walsh, M. Zhang, R. O. Ritchie, A. M. Minor, and M. Asta, Nat. Mater. (to be published).

[3] F. Walsh, M. Asta, and R. O. Ritchie, Proc. Natl. Acad. Sci. **118**, e2020540118 (2021).

[4] F. Walsh, R. O. Ritchie, and M. Asta, Phys. Rev. Mater. **6**, 113602 (2022).

[5] F. Walsh, M. Asta, and L.-W. Wang, npj Comput. Mater. **8**, 186 (2022).

[6] D. de Fontaine, J. Appl. Crystallogr. **4**, 15 (1971).

[7] G. E. Ice and C. J. Sparks, Annu. Rev. Mater. Sci. **29**, 25 (1999).

[8] A. G. Khachaturyan, *Theory of Structural Transformations in Solids* (Dover, Mineola, 2008).

[9] D. D. Johnson, in *Characterization of Materials*, edited by E. N. Kaufmann (Wiley, New York, 2012).

[10] P. Singh, A. V. Smirnov, and D. D. Johnson, Phys. Rev. B **91**, 224204 (2015).

[11] B. Schönfeld *et al.*, Phys. Rev. B **99**, 014206 (2019).

[12] S. Ghosh *et al.*, Phys. Rev. Mater. **6**, 113804 (2022).

[13] A. V. Ceguerra *et al.*, Phys. Rev. B **82**, 132201 (2010).

[14] A. Marucco, J. Mater. Sci. **30**, 4188 (1995).

[15] P. Cenedese, F. Bley, and S. Lefebvre, Acta Crystallogr. A **40**, 228 (1984).

[16] B. Schönfeld *et al.*, Phys. Status Solidi B **148**, 457 (1988).

[17] B. Schönfeld *et al.*, Phys. Status Solidi B **183**, 79 (1994).

[18] K. Inoue, S. Yoshida, and N. Tsuji, Phys. Rev. Mater. **5**, 085007 (2021).

[19] L. Li *et al.*, Acta Mater. **243**, 118537 (2023).

[20] D. de Fontaine, Acta Metall. **23**, 553 (1975).

[21] D. de Fontaine, Metall. Trans. A **12**, 559 (1981).

[22] R. Caudron *et al.*, J. Phys. I **2**, 1145 (1992).

[23] K. Jin *et al.*, Mater. Des. **117**, 185 (2017).

[24] J.-P. Du *et al.*, Acta Mater. **240**, 118314 (2022).

[25] J. B. Staunton, D. D. Johnson, and F. J. Pinski, Phys. Rev. B **50**, 1450 (1994).

[26] A. V. Ruban and M. Dehghani, Phys. Rev. B **94**, 104111 (2016).

[27] P. Papež *et al.*, Mater. Chem. Phys. **304**, 127783 (2023).

[28] M. Fedorov *et al.*, Phys. Rev. B **101**, 174416 (2020).

[29] X. Chen *et al.*, Nature **592**, 712 (2021).

[30] T. Kostiuchenko *et al.*, Phys. Rev. Mater. **4**, 113802 (2020).

[31] F. Otto *et al.*, Acta Mater. **112**, 40 (2016).

[32] F. Sun *et al.*, Acta Mater. **223**, 117487 (2022).

[33] L. Koch *et al.*, J. Appl. Phys. **122**, 105106 (2017).

[34] J. Vrijen *et al.*, Phys. Rev. B **22**, 1503 (1980).

[35] D. de Fontaine, J. Phys. Chem. Solids **34**, 1285 (1973).

[36] J. M. Cowley, J. Appl. Phys. **21**, 24 (1950).

[37] F. X. Zhang *et al.*, Phys. Rev. Lett. **118**, 205501 (2017).

[38] Y. Ma *et al.*, Scripta Mater. **144**, 64 (2018).

[39] H. S. Oh *et al.*, Acta Mater. **216**, 117135 (2021).

[40] B. Yin *et al.*, Nat. Commun. **11**, 2507 (2020).

[41] M. Zhang *et al.*, Acta Mater. **241**, 118380 (2022).
[42] X. Chen *et al.*, Mater. Res. Lett. **10**, 149 (2022).
[43] L. Zhou *et al.*, Acta Mater. **224**, 117490 (2022).
[44] Z. Su *et al.*, Scripta Mater. **212**, 114547 (2022).
[45] M. Zhu *et al.*, Intermetallics **158**, 107896 (2023).
[46] Y. S. Kim, W. Y. Maeng, and S. S. Kim, Acta Mater. **83**, 507 (2015).
[47] J. B. Seol *et al.*, Acta Mater. **194**, 366 (2020).
[48] D. Liu *et al.*, Mater. Today Nano **16**, 100139 (2021).
[49] S. H. Kayani *et al.*, Scripta Mater. **213**, 114642 (2022).
[50] J. B. Seol *et al.*, Nat. Commun. **13**, 6766 (2022).
[51] X. D. Xu *et al.*, Acta Mater. **84**, 145 (2015).
[52] C. Miller, Ph.D. thesis, Colorado School of Mines, 2016.
[53] D. Zhou *et al.*, Scripta Mater. **191**, 173 (2021).
[54] M. Kawamura *et al.*, Acta Mater. **203**, 116454 (2021).
[55] H. Z. Xiao and A. C. Daykin, Ultramicroscopy **53**, 325 (1994).
[56] R. Zhang *et al.*, Nature **581**, 283 (2020).
[57] H.-W. Hsiao *et al.*, Nat. Commun. **13**, 6651 (2022).
[58] D. Cherns, Phil. Mag. **30**, 549 (1974).
[59] H. E. Cook, J. Phys. Chem. Solids **30**, 1097 (1969).
[60] D. L. Bolloc'h, A. Finel, and R. Caudron, Phys. Rev. B **62**, 12082 (2000).
[61] Z. Wu *et al.*, Acta Mater. **81**, 428 (2014).
[62] B. Gludovatz *et al.*, Nat. Commun. **7**, 10602 (2016).
[63] G. Laplanche *et al.*, Acta Mater. **128**, 292 (2017).
[64] A. Tamm *et al.*, Acta Mater. **99**, 307 (2015).
[65] J. Ding *et al.*, Proc. Natl. Acad. Sci. **115**, 8919 (2018).
[66] L. Zhang *et al.*, Scripta Mater. **136**, 78 (2017).
[67] D. Billington *et al.*, Phys. Rev. B **102**, 174405 (2020).
[68] B. C. Sales *et al.*, Sci. Rep. **6**, 26179 (2016).
[69] C. Niu *et al.*, Appl. Phys. Lett. **106**, 161906 (2015).
[70] Z. Pei *et al.*, npj Comput. Mater. **6**, 122 (2020).
[71] Q.-J. Li, H. Sheng, and E. Ma, Nat. Commun. **10**, 3563 (2019).
[72] B. C. Sales *et al.*, npj Quantum Mater. **2**, 33 (2017).
[73] A. Zunger *et al.*, Phys. Rev. Lett. **65**, 353 (1990).
[74] C. G. Robbins, H. Claus, and P. A. Beck, Phys. Rev. Lett. **22**, 1307 (1969).
[75] S. N. Khan, J. B. Staunton, and G. M. Stocks, Phys. Rev. B **93**, 054206 (2016).
[76] C. Niu *et al.*, Nat. Commun. **9**, 1363 (2018).
[77] J. Miao *et al.*, Acta Mater. **132**, 35 (2017).
[78] D. Liu *et al.*, Science **378**, 978 (2022).
[79] L. Rémy and A. Pineau, Mater. Sci. Eng. **26**, 123 (1976).
[80] F. Mustafa *et al.*, Materials **16**, 1044 (2023).
[81] O. Mohamed, M. Egilmez, and W. Abuzaid, Appl. Phys. A **128**, 221 (2022).
[82] H. W. Deng *et al.*, J. Alloys Compd. **899**, 163349 (2022).
[83] T. A. Elmslie *et al.*, Phys. Rev. B **106**, 014418 (2022).
[84] P. Nash, Bull. Alloy Phase Diagr. **7**, 466 (1986).
[85] A. Marucco and B. Nath, J. Mater. Sci. **23**, 2107 (1988).
[86] D.-G. Park *et al.*, J. Magn. Magn. Mater. **272-276**, e1715 (2004).
[87] R. J. Taunt and B. Ralph, Phys. Status Solidi A **29**, 431 (1975).
[88] J. Crangle and G. M. Goodman, Proc. R. Soc. Lond. A **321**, 477 (1971).
[89] M. J. Besnus, Y. Gottehrer, and G. Munschy, Phys. Status Solidi B **49**, 597 (1972).
[90] S. Vishvakarma and V. Srinivas, J. Phys. Condens. Matter **33**, 205803 (2021).
[91] S. Arajs, J. Appl. Phys. **38**, 2946 (1967).
[92] M. Hirabayashi *et al.*, Trans. Jpn. Inst. Met. **10**, 365 (1969).
[93] A. V. Ruban *et al.*, Phys. Rev. B **75**, 054402 (2007).
[94] Z. Dong *et al.*, Phys. Rev. B **96**, 174415 (2017).
[95] Z. Dong *et al.*, Appl. Phys. Lett. **119**, 081904 (2021).

[96] A. Arya *et al.*, Acta Mater. **50**, 3301 (2002).

[97] J. D. Tucker, Ph.D. thesis, University of Wisconsin-Madison, 2008.

[98] J. S. Wróbel *et al.*, Phys. Rev. B **91**, 024108 (2015).

[99] J. G. Goiri and A. Van der Ven, Acta Mater. **159**, 257 (2018).

[100] S. Curtarolo *et al.*, Comput. Mater. Sci. **58**, 227 (2012).

[101] A. Jain *et al.*, APL Mater. **1**, 011002 (2013).

[102] M. Rahaman, B. Johansson, and A. V. Ruban, Phys. Rev. B **89**, 064103 (2014).

[103] G. Kresse and J. Hafner, Phys. Rev. B **47**, 558 (1993).

[104] G. Kresse and J. Furthmüller, Phys. Rev. B **54**, 11169 (1996).

[105] G. Kresse and J. Furthmüller, Comput. Mater. Sci. **6**, 15 (1996).

[106] M. Methfessel and A. T. Paxton, Phys. Rev. B **40**, 3616 (1989).

[107] W. Tang, E. Sanville, and G. Henkelman, J. Phys. Condens. Matter **21**, 084204 (2009).

[108] J. P. Perdew and A. Zunger, Phys. Rev. B **23**, 5048 (1981).

[109] D. M. Ceperley and B. J. Alder, Phys. Rev. Lett. **45**, 566 (1980).

[110] J. P. Perdew, K. Burke, and M. Ernzerhof, Phys. Rev. Lett. **77**, 3865 (1996).

[111] J. P. Perdew *et al.*, Phys. Rev. Lett. **100**, 136406 (2008).

[112] S. H. Vosko, L. Wilk, and M. Nusair, Can. J. Phys. **58**, 1200 (1980).

[113] Edited by W. M. Haynes, *CRC Handbook of Chemistry and Physics*, 97th ed. (CRC, Boca Raton, 2016).

[114] R. Hafner *et al.*, Phys. Rev. B **65**, 184432 (2002).

[115] E. Fawcett, Rev. Mod. Phys. **60**, 209 (1988).

[116] L. M. Sandratskii, Adv. Phys. **47**, 91 (1998).

[117] S. Blundell, *Magnetism in Condensed Matter* (OUP, Oxford, 2001).

[118] I. Turek *et al.*, Phil. Mag. **86**, 1713 (2006).

[119] L. Barnard *et al.*, Acta Mater. **81**, 258 (2014).

[120] E. Fawcett *et al.*, Rev. Mod. Phys. **66**, 25 (1994).

[121] W. Schweika and H.-G. Haubold, Phys. Rev. B **37**, 9240 (1988).

[122] P. Pietrokowsky, Nature **206**, 291 (1965).

[123] K. K. Murata and S. Doniach, Phys. Rev. Lett. **29**, 285 (1972).

[124] M. Uhl and J. Kübler, Phys. Rev. Lett. **77**, 334 (1996).

[125] N. M. Rosengaard and B. Johansson, Phys. Rev. B **55**, 14975 (1997).

[126] S. L. Dudarev and P. M. Derlet, J. Comput.-Aided Mater. Des. **14**, 129 (2007).

[127] A. V. Ruban *et al.*, Phys. Rev. B **70**, 125115 (2004).

[128] F. Körmann *et al.*, J. Phys. Condens. Matter **25**, 425401 (2013).

[129] D. J. Singh and J. Ashkenazi, Phys. Rev. B **46**, 11570 (1992).

[130] M. Yu. Lavrentiev *et al.*, J. Appl. Phys. **120**, 043902 (2016).

[131] L. Vitos, P. A. Korzhavyi, and B. Johansson, Phys. Rev. Lett. **96**, 117210 (2006).

[132] Z. Dong and L. Vitos, Scripta Mater. **171**, 78 (2019).

[133] H. Masumoto, M. Sugihara, and M. Takahashi, J. Jpn. Inst. Met. **18**, 85 (1954).

[134] Y. Z. Vintaykin, V. P. Itkin, and B. M. Mogutnov, Phys. Met. Metallogr. **33**, 167 (1972).

[135] V. I. Goman'kov *et al.*, Phys. Met. Metallogr. **14**, 25 (1962).

[136] Z. I. Alizade and A. A. Kerimov, Sov. Phys. J. **14**, 231 (1971).

[137] V. I. Chechernikov and J. Pop, Phys. Met. Metallogr. **17**, 164 (1964).

[138] H. Mamiya *et al.*, J. Alloys Compd. **681**, 367 (2016).

[139] S. V. Halilov *et al.*, Europhys. Lett. **39**, 91 (1997).

[140] F. Körmann *et al.*, Phys. Rev. B **81**, 134425 (2010).

[141] F. Körmann *et al.*, Phys. Rev. B **83**, 165114 (2011).

[142] F. Körmann *et al.*, Phys. Rev. B **78**, 033102 (2008).

[143] F. Körmann *et al.*, Phys. Rev. Lett. **113**, 165503 (2014).

[144] R. F. L. Evans, U. Atxitia, and R. W. Chantrell, Phys. Rev. B **91**, 144425 (2015).

[145] C. H. Woo *et al.*, Phys. Rev. B **91**, 104306 (2015).

[146] L. Bergqvist and A. Bergman, Phys. Rev. Mater. **2**, 013802 (2018).

[147] J. Barker and G. E. W. Bauer, Phys. Rev. B **100**, 140401 (2019).

[148] A. W. Sandvik, AIP Conf. Proc. **1297**, 135 (2010).

[149] F. Körmann, Ph.D. thesis, Paderborn University, 2011.

[150] M. Takasu, S. Miyashita, and M. Suzuki, in *Quantum Monte Carlo Methods in Equilibrium and Nonequilibrium Systems*, edited by M. Suzuki (Springer-Verlag, Berlin, 1986).

[151] P. Henelius and A. W. Sandvik, Phys. Rev. B **62**, 1102 (2000).

[152] A. W. Sandvik, Phys. Rev. E **68**, 056701 (2003).

[153] G. A. Raggio, J. Phys. A **39**, 617 (2006).

[154] J. Anders and V. Vedral, Open Syst. Inf. Dyn. **14**, 1 (2007).

[155] L. Amico *et al.*, Rev. Mod. Phys. **80**, 517 (2008).

[156] R. F. Werner, Phys. Rev. A **40**, 4277 (1989).

[157] M. E. Fisher, Am. J. Phys. **32**, 343 (1964).

[158] M. Månson, Phys. Rev. B **12**, 400 (1975).

[159] P.-W. Ma, C. H. Woo, and S. L. Dudarev, Phys. Rev. B **78**, 024434 (2008).

[160] N. B. Melnikov, G. V. Paradezhenko, and B. I. Reser, J. Magn. Magn. Mater. **473**, 296 (2019).

[161] H. A. Mook, J. W. Lynn, and R. M. Nicklow, Phys. Rev. Lett. **30**, 556 (1973).

[162] J. W. Lynn, Phys. Rev. B **11**, 2624 (1975).

[163] H. Capellmann and V. Viera, Solid State Commun. **43**, 747 (1982).

[164] V. Heine, A. I. Liechtenstein, and O. N. Mryasov, Europhys. Lett. **12**, 545 (1990).

[165] N. B. Melnikov, B. I. Reser, and G. V. Paradezhenko, AIP Adv. **8**, 101402 (2018).

[166] N. B. Melnikov and B. I. Reser, Phys. Met. Metallogr. **117**, 1328 (2016).

[167] V. I. Manousiouthakis and M. W. Deem, J. Chem. Phys. **110**, 2753 (1999).

[168] F. Wang and D. P. Landau, Phys. Rev. Lett. **86**, 2050 (2001).

[169] G. Chaddha and M. S. Seehra, Solid State Commun. **44**, 1097 (1982).

[170] C. G. Windsor and R. W. H. Stevenson, Proc. Phys. Soc. **87**, 501 (1966).

[171] J.-S. Wang and R. H. Swendsen, Phys. A **167**, 565 (1990).

[172] H. J. F. Jansen, K. B. Hathaway, and A. J. Freeman, Phys. Rev. B **30**, 6177 (1984).

[173] J. Yin *et al.*, Phys. Rev. B **86**, 214423 (2012).

[174] S. Mankovsky, S. Polesya, and H. Ebert, Phys. Rev. B **102**, 134434 (2020).